EXPERIMENTAL STUDIES IN NON-EQUILIBRIUM PHYSICS

by

John Robert Cressman, Jr.

Submitted to the Graduate Faculty of
the Department of Physics and Astronomy in partial fulfillment
of the requirements for the degree of

Doctor of Philosophy

University of Pittsburgh

2003

UNIVERSITY OF PITTSBURGH

Department of Physics and Astronomy

This dissertation was presented

by

John Robert Cressman, Jr.

It was defended on

August 20th 2003

and approved by

Walter I. Goldburg, Departament of Physics and Astronomy

Carson Chow, Department of Mathematics

Rob Coalson, Department of Chemistry

Yadin Goldschmidt, Department of Physics and Astronomy

Xioa lun Wu, Department of Physics and Astronomy

Dissertation Advisor: Walter I. Goldburg, Departament of Physics and Astronomy

EXPERIMENTAL STUDIES IN NON-EQUILIBRIUM PHYSICS

John Robert Cressman, Jr., Ph. D.

University of Pittsburgh, 2003

This work is a collection of three experiments aimed at studying different facets of non-equilibrium dynamics. Chapter I concerns strongly compressible turbulence, which turns out to be very different from incompressible turbulence. The focus is on the dispersion of contaminants in such a flow. This type of turbulence can be studied, at very low mach number, by measuring the velocity fields of particles that float on a turbulently stirred body of water. It turns out that in the absence of incompressibility, the turbulence causes particles to cluster rather than to disperse. The implications of the observations are far reaching and include the transport of pollutants on the oceans surface, phytoplankton growth, as well as industrial applications.

Chapter II deals with the effects of polymer additives on drag reduction and turbulent suppression, a well-known phenomenon that is not yet understood. In an attempt to simplify the problem, the effects of a polymer additive were investigated in a vortex street formed in a flowing soap film. Measurements suggest that an increase in elongational viscosity is responsible for a substantial reduction in periodic velocity fluctuations. This study also helps to illuminate the mechanism responsible for vortex separation in the wake of a bluff body.

Chapter III describes an experiment designed to test a theoretical approach aimed at generalizing the classical fluctuation dissipation theorem (FDT). This theorem applies to systems driven only slightly away from thermal equilibrium, whereas ours, a liquid crystal undergoing electroconvection, is so strongly driven, that the FDT does not apply. Both theory and experiment focus on the flux in global power fluctuations. Physical limitations did not permit a direct test of the theory, however it was possible to establish several interesting

characteristics of the system: the source of the fluctuations is the transient defect structures that are generated when the system is driven hard. It is found that the power fluctuations are spatially uncorrelated, but strongly correlated in time and even quasi-periodic.

TABLE OF CONTENTS

LIST OF FIGURES

PREFACE

Understanding is not the ability to predict, nor is it a proof. In fact it can be completely wrong or degenerate. The earth used to be the center of the universe, flat and travelling through an ether. It comes through experience, knowledge, logic and thought, but these are not enough. Understanding only occurs when the combination of these elements is formed into a single concept that can either be de-constructed into already excepted forms or more importantly by excepting something new as an element of ones existence. Understanding is a powerful tool, but more importantly it is the essential state of thought that brings our minds in contact with existence; the sensation of knowing.

Is it possible to fully comprehend our existence? I don't know, but our inability to frame an intuitive picture of non-linear systems shows that we still have a lot of work to do. Even if we manage to solve mathematically or numerically the Navier-Stokes equation in all of its incarnations, will we understand turbulence?

The study of non-equilibrium systems is difficult for many reasons. Although we are often able to write down mathematical expressions that govern such systems, analytical solutions are usually inaccessible. However, in my view, the main difficulty is not the lack of rigorous theoretical guidance, rather it lies in our conceptual approach to the problem.

Our understanding of the world is constructed from an ensemble of concepts with which we are comfortable. Ideas that are grounded in common experience, such as objects, interaction (causality) periodicity, and probabilities. A set of elements chosen out of necessity for survival not maximal understanding.

If such simple concepts abound in non-linear systems they have limited overlap with our usual set of tools. This is not to say that non-linear system are devoid of structure. In fact the degree of structure seen in turbulent systems is astounding. I only propose that given

a different conceptual basis these systems may become far less complex and perhaps within our scope of understanding.

The experiments discussed here were devised to study specific problems in turbulence and non-equilibrium statistical mechanics. Although their motivation was far more grounded than the lofty goals outlined above, I have benefited greatly from the subtle connections I have witnessed while exposing myself to these systems.

I am greatly indebted to my advisor Walter Goldburg, who has taught me much more than I could learn. A superb scientist and an excellent human, I will miss working in his lab.

I would like to thank my parents for providing me with the structure for thought, and the freedom for imagination. Their love and support has always given me peace and stability.

1.0 INTRODUCTION

Many natural systems are non-linear, from slow rock formation to plant growth to the motion of air and water. It is more difficult to find behavior that is truly linear. It is not surprising however, that most of our knowledge of the world is derived through linear analysis. The concept of our surroundings as objects and interactions is born out in our language, logic and thought. Even in complex systems one attempts to isolate structure.

The work presented here, although quite diverse, all deals to some degree with the structure found in non-linear systems. In such systems it is often quite difficult to define what is meant by structure. These systems range from turbulent to chaotic, with varying degrees of complexity. In each case an attempt is made to isolate relevant scales and refine these ideas to objects and periods were possible.

In chapter I the motion of tracer particles spread across the surface of a turbulent fluid is investigated. The main focus of this study is to determine how compressibility alters the dispersive nature of a turbulent fluid. In addition, the effects of compressibility on the structure of turbulence is investigated. Although turbulence is not a good candidate for reduction into definable objects, vortices fall short, structure still abounds in a statistical sense, revealed in spatiotemporal measurements of the velocity field.

In chapter II the effects of a long chain polymer additive to a quasi-two-dimensional vortex street are studied. A vortex street is produced by the passage of a fluid past a bluff body, in this case a cylindrical rod(see figure 12.) In the absence of the polymer additive the vortex street displays temporal and spatial structure. At least in the near field(close to the rod), vortices behave as well-defined objects, and a sharply defined shedding frequency(vortex creation rate) exists. The addition of the polymer acts to greatly alter the vortex street both temporally and spatially.

Although this system lacks a precise mathematical solution, one can explain this phenomena by the presence of a shear instability downstream of the rod. This instability is responsible for inducing velocity fluctuations necessary to create the vortex street. The addition of the polymer effects the location and strength of the instability which in turn produces drastic changes in the flow structure.

The final experiment deals with the fluctuations in power injected into a liquid crystal. Here it is possible to define structures in the flow responsible for fluctuations in power as well as measure their average lifetime. The complexity of this system is easily tuned, and a transition from identifiable objects to a more statistical interpretation is quantified.

In addition contact is made with a promising theory that extends the treatment of equilibrium statistical mechanics to non-equilibrium systems. Here again use is made of the idea of a dynamical object through which one can assign a dynamical temperature.

2.0 COMPRESSIBLE TURBULENCE

2.1 INTRODUCTION

Most turbulence studies deal with fluids, including water and air, that maintain a static uniform density throughout. If the relative velocity of a fluid element exceeds a critical speed c, the speed of sound, spatiotemporal fluctuations in density will occur. The presence of these density fluctuations is what defines a compressible system. It turns out however that high flow speeds are not necessary to produce these fluctuations. Here we investigate the effects of compressibility on a fluid's ability to disperse particles as well as establish whether the well-documented structure found in incompressible flow is altered.

Everyone is familiar with the process of turbulent mixing. From stirring cream into coffee, to attempting to recover the contents of a dropped notebook on a windy day; rapid chaotic dispersion is, to many, the main qualitative aspect of turbulence. Many processes in nature depend on the mechanism of turbulent diffusion. For example the dispersal of pollen, the spread of dust, essential for rain formation, and the dilution of contaminants[1, 2].

It is striking then to find that by making the flow strongly compressible, one can cripple this mixing effect. It can cause an initially uniform distribution of particles to coagulate under the action of stirring. In this work strong compressibility is evident in the motion of small particles that float on a turbulent body of water as seen in Fig. 1. This photo, was taken a fraction of a second after the particles were uniformly dispersed. It is clear that coagulation can manifest itself in many ways, influencing the dispersal of pollutants on the sea and the growth of phytoplankton there [3, 4].

This image(see also figure 7) captures the dominant qualitative characteristics of the flow: small gaps are created in the initially uniform distribution of particles. These voids grow

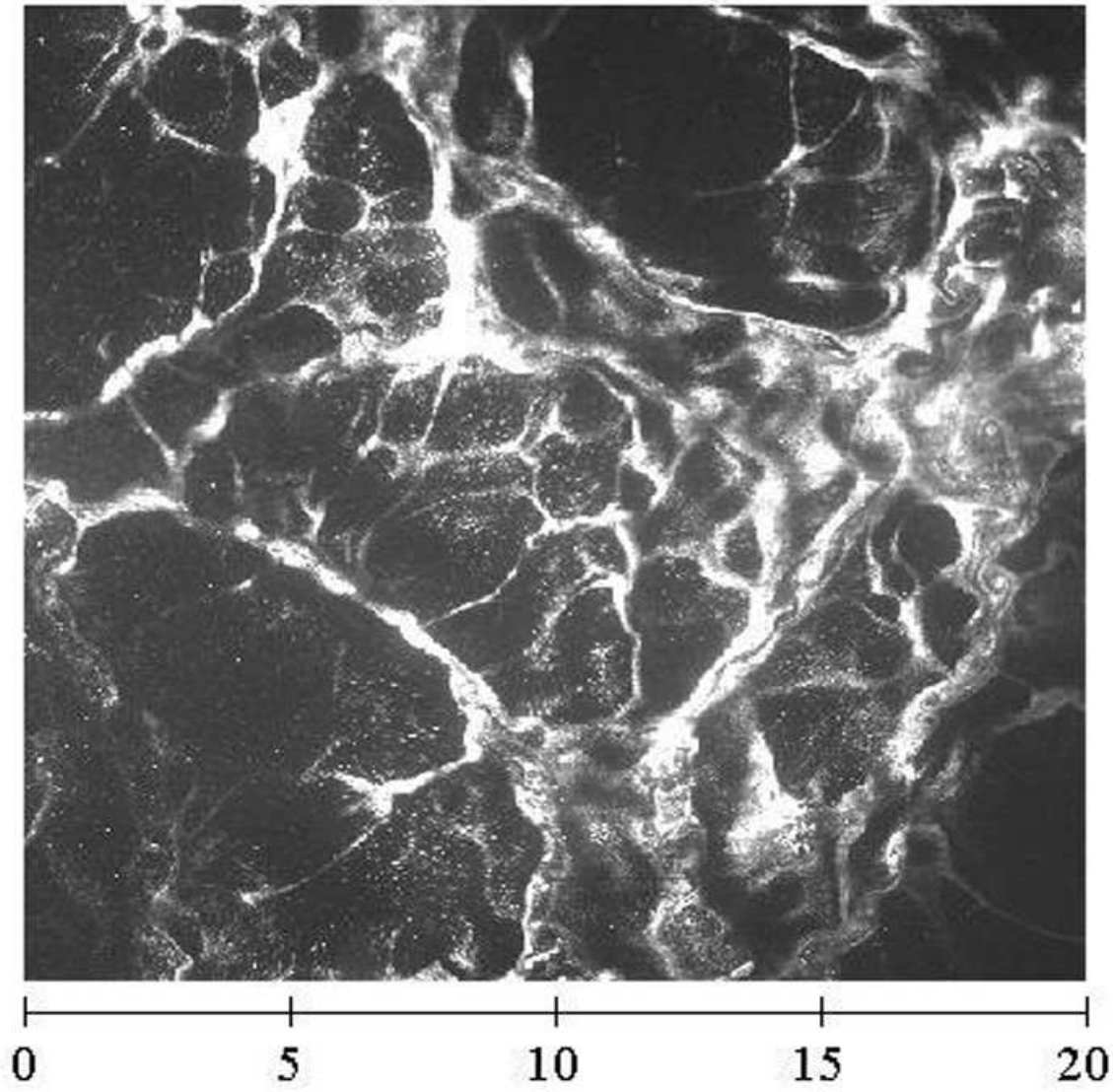

Figure 1: Image of a cloud of particles on the surface of a turbulent body of water. The particles which are 10 μm in diameter appear as white and were initially dispersed uniformly over the surface. This image was captured 100 ms later. The scale below the figure is in cm.

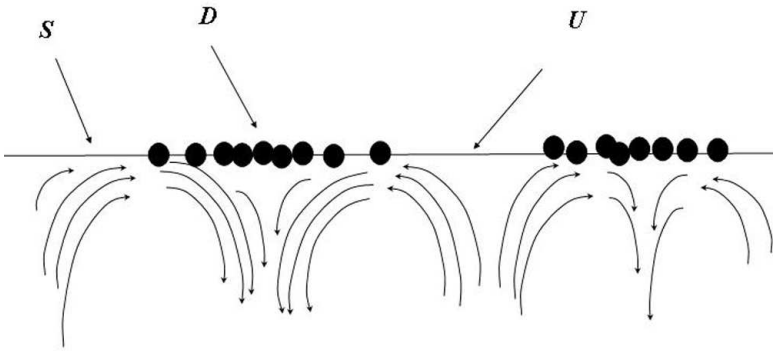

Figure 2: Cartoon illustrating the mechanism for particle coagulation. Particles collect at downwellings(D) and spread away form upwellings (U).

very quickly as the particles are forced nearly radially outward from the center of bursts of fluid impinging on the surface. The field evolves, until the entire distribution is forced into one of two structures; either thin ribbons, or less dense patches of tracers that form at the intersections (or vertices) of ribbons. The particles will eventually be forced to the sides of the tank by the presence of relatively stronger turbulence at the center.

The origin of the coagulation is apparent in Fig. 2. The incompressible fluid below the surface is shown to be moving upward near point U and downward near point D on the surface S. The floaters cannot follow the bulk motion; rather they accumulate at points like D and flee points like U. The floating particles move in the $x - y$ plane, which will be taken as $z = 0$. They simply sample the horizontal components of the flow velocity, $v_x(x, y, 0, t)$ and $v_y(x, y, 0, t)$, of the incompressible fluid below them. Since water is incompressible, the divergence of the velocity field is zero at all points on the surface and below it, so that $\partial v_x(x, y, z, t)/\partial x + \partial v_y(x, y, z, t)/\partial y = -\partial v_z(x, y, z, t)/\partial z$, which is non-zero and, in fact, large. Thus the floaters form a two-dimensional compressible subsystem, even though the flow velocity is negligible compared to the speed of sound of the water below.

Recently, compressible turbulence has come under theoretical scrutiny and has been studied in computer simulations [5]. Numerical studies performed by Joerg Schumacher, and Bruno Eckhardt proved extremely fruitful. Comparisons between experimental and numerical work will be discussed and a brief description of the simulation is given in Appendix C.

This chapter is in four parts, beginning with a brief description of ideal flow, followed by a presentation of the experimental setup, experimental results, and a discussion of these measurements to illustrate the unique aspects of this flow. The chapter concludes with a discussion of the results.

Several important parameters used to describe the flow are defined as they appear in the text. However a thorough discussion of their meaning and experimental resolution is contained in Appendix A.

The methods of acquisition and analysis of data are presented in Appendix B. The presence of surface contaminants greatly effects the results presented here, and significant effort was applied to remove these effects. A discussion of these effects is incongruent with our focus, and is left to Appendix D.

2.2 IDEAL TURBULENT FLOW

In order to appreciate the unique aspects of the flow studied here, it is helpful to first review what is considered typical, or as will be referred to here as ideal turbulence. The governing equation for many fluids, including water and air is the Navier-Stokes (NS) equation:

$$\partial \mathbf{u}/\partial + \mathbf{u} \cdot \nabla \mathbf{u} = -\nabla p/\rho + \nu \nabla^2 \mathbf{u} + f \tag{2.1}$$

The NS equation is simply Newton's Second Law for a small element of fluid within a continuum. The mass of the element has been divided out. The left hand side is the full time derivative of the velocity and the terms on the r.h.s are the forces acting on the fluid element. Here p is the pressure acting on the fluid element, ρ is the density of the fluid and ν is the kinematic viscosity. If the fluid is incompressible the NS equation is supplemented with $\nabla \cdot \mathbf{u} = 0$ providing a fourth equations for four unknowns. This system of nonlinear

partial differential equations can only be solved exactly for the simplest geometries(boundary conditions). It is not yet possible to solve these equations for turbulent flows, however by studying time averages of the variables in the NS equation one can still derive powerful results.

The underpinnings of turbulent theory are based on several assumptions. Translational invariance, rotational invariance, and time invariance are all lost in a dynamical sense as a flow becomes unstable through external forcing. These symmetries, however, are reattained in a statistical sense if the flow is driven into a highly turbulent state. Therefore, it is natural to investigate turbulent phenomena in a statistical manner[6].

Although the details of the complex dynamics are lost through averaging it is possible to ascertain the spatial structure of the flow. A second assumption is that the dissipative effects of viscosity only act at very small scales. Energy is injected into a flow at a scale, L, and is removed from the fluid at a much smaller scale η. The scale L is essentially the spatial extent of the mechanism responsible for exerting a force on a fluid, i.e. the diameter of a rod placed in a flow. Dissipation occurs at scales where Δv_r, the velocity differences on a separation r, grows linearly with the separation. In the dissipative range, molecular diffusion is responsible for converting coherent velocities (modes) into random heat.

Since the system is in a steady state, all of the energy injected must also be dissipated. Energy is only added at the injection scale, and removed at the dissipative scale. Another aspect of a turbulent system is that the energy flowing through a given scale is deposited or removed from very similar scales. This trait is referred to in the literature as locality[6]. Therefore there must be a loss-free transfer of energy through all intermediate scales, the so called inertial range. This gives rise to a constant flow of energy through the inertial range. The only conserved quantity for three-dimensional turbulence is this flow rate, or injection/dissipation rate, $\epsilon(cm^2/s^3)$.

By assuming that viscosity plays a negligible role in the inertial range a dimensional argument can be used to show that the third moment of velocity differences, $D_3(r) = \langle(\Delta v_r)^3\rangle$ depends on ϵ and the separation r alone. Dimensional analysis gives $\langle(\Delta v_r)^3\rangle \simeq (\epsilon r)$. The brackets denote a spatial average. Using the assumptions of isotropy, homogeneity, and incompressibility Kolmogorov derived an exact expression for the third moment. The famous

4/5 law equates the third moment to -4/5ϵr[7]. The third moment, consisting of a product of a velocity and a velocity squared, can be interpreted as the energy flux on a scale r.

Landau argued that ϵ is dependent on drive and geometry, and should not be universal. A simple argument[6] shows that all moments except for the third are nonlinear in ϵ which depends strongly on the way energy is injected into the flow. In other words the following relation, $\overline{\epsilon}^n = \overline{\epsilon^n}$ only holds for n = 1 due to the dependence of ϵ on time and space varying forcing. Here the bar refers to an average over either time or space. Therefore, moments other than the third moment will not scale as in the Kolmogorov prediction, and may be sensitive to drive and geometry. Experiments show that deviations from the predicted scaling laws do occur for higher moments of the velocity differences.

The discrepancy is usually attributed to particulary strong and isolated events referred to as intermittent. In three-dimensional turbulence, velocity gradients can cause a rapid and strong increase in the curl of the velocity field, a mechanism called vortex stretching(This behavior is not present in two-dimensional turbulence, and the mean squared vorticity, is a second conserved quantity). Intermittency effects the structure function by increasing the relative velocity differences at small scales hence lower the scaling exponent. This effect is only pronounced for higher order structure functions.

The results for the average spatial structure can be extended to predict the dispersive nature of ideal turbulence. In this case the quantity of interest is the separation $\Delta(t)$ of two points in the flow where,

$$\langle \frac{d\Delta^2}{dt} \rangle = 2\langle \mathbf{\Delta(t)} \cdot \mathbf{dV(t)} \rangle \tag{2.2}$$

Here $\mathbf{dV}$ is the relative velocity of the two points separated by Δ. Inserting $\Delta(t) = \Delta(0) + \int_0^t dV(\tau)d\tau$ into 2.2 gives

$$\langle \frac{d\Delta^2}{dt} \rangle = 2\langle \mathbf{\Delta(0)} \cdot \mathbf{dV(t)} \rangle + 2\int_0^t \langle dV(\tau)dV(t) \rangle d\tau \tag{2.3}$$

For separations larger than η, the relative velocity quickly looses memory of its initial position making the first term on the r.h.s much smaller than the second. The second term can be shown to be proportional to $\langle \mathbf{dV(t)} \cdot \mathbf{dV(t)} \rangle t_\Delta$, where t_Δ is some relevant time scale[8]. Here we will take t_Δ to be the eddy turn over time $\Delta/|\mathbf{dV}|$. Inserting this into 2.3, and using

the Kolmogorov prediction for velocity differences, we arrive at the well-known Richardson result for separations within the inertial range.

$$\langle \frac{d\Delta^2}{dt} \rangle \simeq \langle \mathbf{dV(t)}^2 \rangle \Delta / |\mathbf{dV}| \simeq \Delta^{4/3}. \tag{2.4}$$

Integration gives $\Delta^2 \simeq t^\alpha$, where $\alpha = 3$.

Once the particle pairs become separated by distances larger than the outer scale l_0 their velocities become uncorrelated, and their dispersion becomes Brownian, making $\alpha = 1$. If the particles experience projectile-like motion, where the particle velocity is constant in time making the separation grow linearly in time, the exponent α is equal to 2.

2.3 EXPERIMENT

Several difficulties arise when attempting to study turbulent systems. As in all experiments, in order to make contact with theoretical predictions experiments must be made to coincide as closely as possible with the postulates of the theory. Whereas the conceptual difficulty in studying turbulence is its enormous complexity the physical realization is often quite the opposite. Large scale structures often persistent producing a high degree of anisotropy.

Theoretically one assumes that every point in turbulent flow behaves the same on average (homogeneity), and the structure of the flow is the same when viewed from all directions (isotropy). These two restrictions are often essential for deriving properties of a flow.

Experimental turbulence is generally created by forcing a fluid through a geometric constriction (closed flow) such as wind tunnels experiments or conversely by forcing a fluid around a geometric structure (open flow) as in the case of a spinning propeller. In either case the structure of the turbulence will contain, or remember, if only for a short time and distance, the nature of its creation, making truly isotropic, homogenous turbulence very difficult to achieve. However, for a given geometry, the more turbulent a system is, the closer it approaches the limits of homogeneity and isotropy. A measure of the degree of a turbulence is the Reynold's Number, which is defined in detail in Appendix A.

In order to isolate the effects of compressibility substantial effort was applied to make the

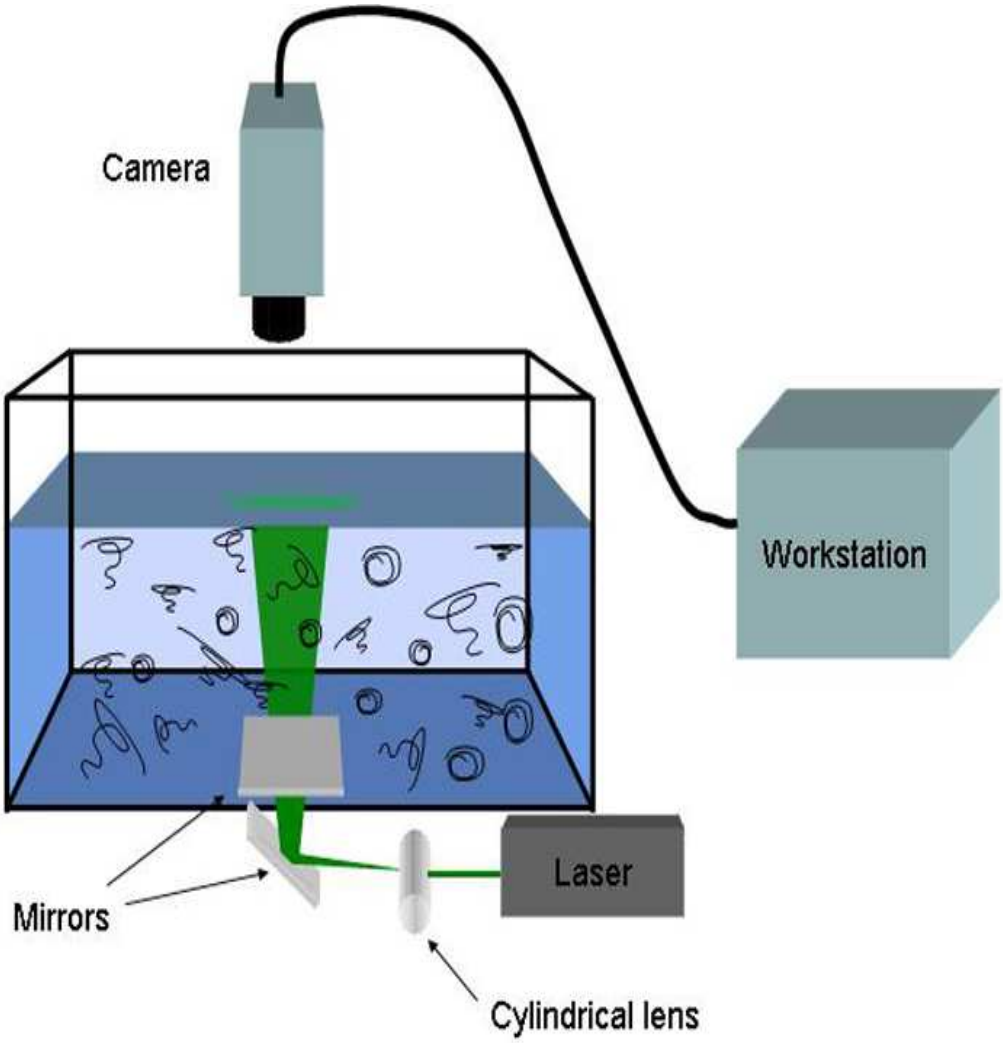

Figure 3: Two mirrors along with a cylindrical lens are used to produce a sheet of laser light at the surface of a large tank. A camera positioned above the tank is used to image the surface flow, and transmit data to a workstation for analysis.

flow as homogeneous, and isotropic as possible in the plane of the surface. The appearance of waves, make it impossible to arbitrarily increase the Reynold's Number. Therefore homogeneity and isotropy were maximized by varying the forcing both temporally and spatially as will now be discussed.

Great care was taken to make a large surface available for experimental investigation. All of the experiments reported here were performed in a large water tank as shown in figure 3. The tank (of lateral dimension of 1 m) was typically filled to a depth of 30 cm. Initially a large grid was used to stir the bulk fluid. All the parameters used in our setup were typical of prior oscillating grid experiments [9], except that the lateral dimensions of our tank were somewhat larger. The grid was driven sinusoidally at a frequency of 4.5 $\pm$0.3 Hz from above by a 1/4 hp motor. The vertical amplitude of grid motion was A = 1.25 cm. These parameters were varied by only a small amount, but the distance Z between the grid and the water surface defined as $Z = 0$, was rather widely varied. Reducing Z increases the Reynolds number of the turbulence on the surface and near it.

In order to minimize surface waves, and eliminate a large toroidal flow produced by flexing of the grid, a second system was implemented. The oscillating grid was replaced by an array of rotating nozzles as shown in figure 4. Thirty six pairs of nozzles are used to mix the bulk flow. Eight valves, located on either side of the pipe array, are used to "balance" the turbulent intensity throughout the tank. This scheme effectively removes any large scale flow in the tank.

The nozzles are positioned at an angle of approximately 45 degrees upward with respect to the plane of the surface. This geometry was found to produce strong turbulence at the surface, without producing significant surface deflections. The jets rotate at a frequency of a few hertz. With this scheme the visual obstructions produced by the grid supports were removed. The entire surface is therefore fully available for visual, and video inspection. The velocity field was measured by spreading small buoyant particles on the surface. A wide variety of particles was used including hollow glass spheres (10 μm to 200 μm), mushroom spores (50 μm), and talcum powder (10 μm). For more details see Appendix B.

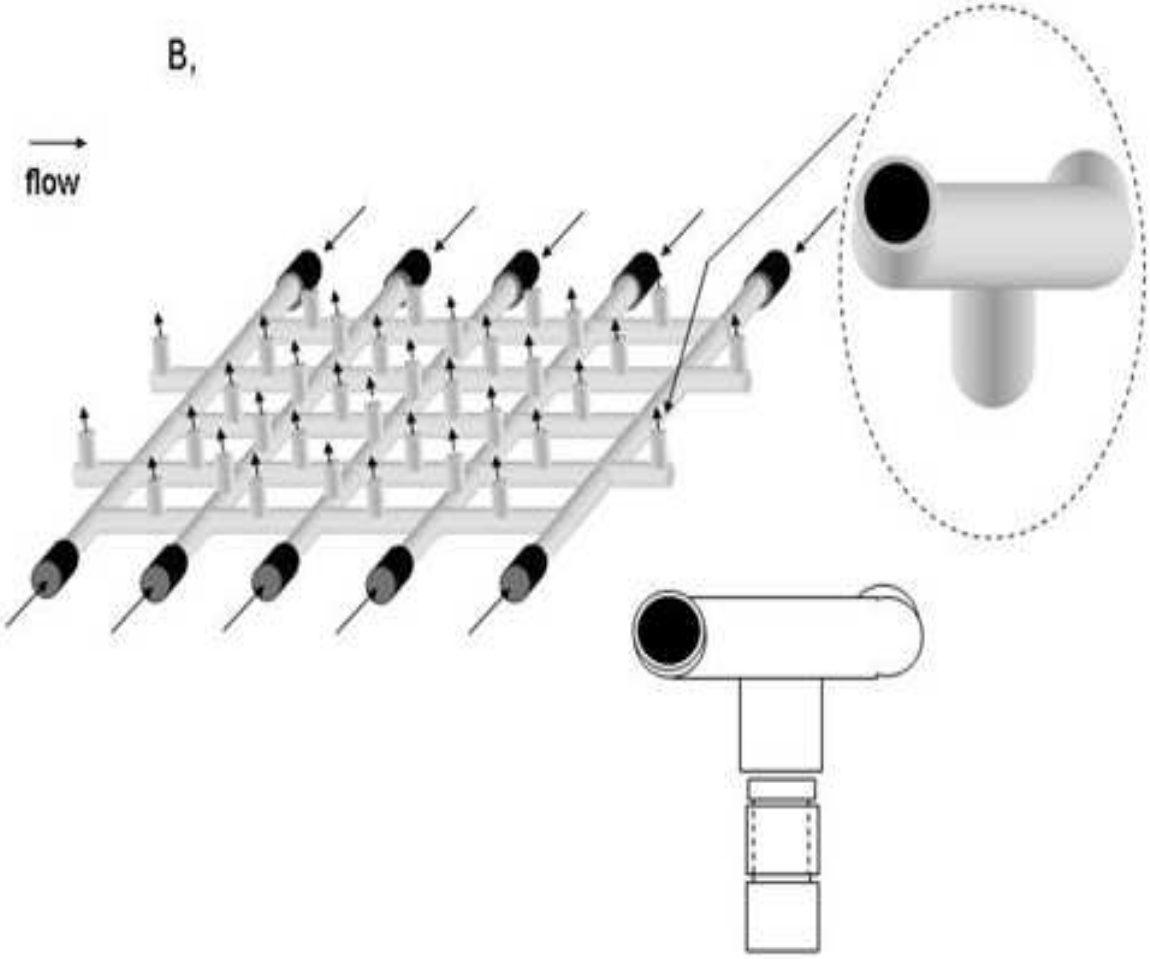

Figure 4: Drawing of the array of jets. A blow up of a nozzle is seen on the right. For clarity the jets are not shown on the grid of pipes. The flow direction is indicated with arrows, and a nozzle is placed on top of the vertical pipes where the flow exits the array. The lower picture shows the construction of a rotating nozzle.

2.4 EXPERIMENTAL RESULTS

In the following section the results of several studies are presented. On the practical side pair measurement were performed in order to provide essential information about the dispersion of a passive scalar on a the surface of a turbulent fluid. The fundamental effects of compressibility were studied by investigating established quantities from incompressible turbulence in order to isolate specific effects of compression.

2.4.1 Eulerian measurements

Until recently it has been very difficult, especially in three-dimensions, to experimentally track the motion of particles in a turbulent fluid for any significant length of time. For this reason, the bulk of turbulent data is based on measurements of a velocity field at a point, or points, in space. Several techniques including particle imaging velocimetry are able to capture an entire velocity field measured over a very short time. Even simpler techniques including hot wire anemometry, and laser doppler velocimetry only measure the velocity at a single point. In order to extract spatial information one makes use of the assumption that the flow doesn't evolve appreciably in the time it takes a large mean flow to move it past a probe. In this way velocities separated in time can be interpreted as spatially displaced. All of these measurements are aimed at investigating the velocity field in the laboratory frame, and are called Eulerian measurements. The drawback of this analysis is the lack of temporal information, which requires significantly more complex data acquisition and analysis.

By measuring the static velocity field we hoped to investigate any interesting effects on spatial correlations imposed by the geometric confinement of particles on the surface. Being comprised of particles constrained to the surface their motion is qualitatively different from that of the water molecules in the bulk fluid. Although the fluid is incompressible, the inability of the floaters to enter the bulk flow assures that they will have a nonzero two-dimensional divergence, as demonstrated in Fig. 2.

Direct measurements of the velocity field establish that the surface is not two-dimensionally incompressible. In Figure 5 we present measurements of the probability density function of

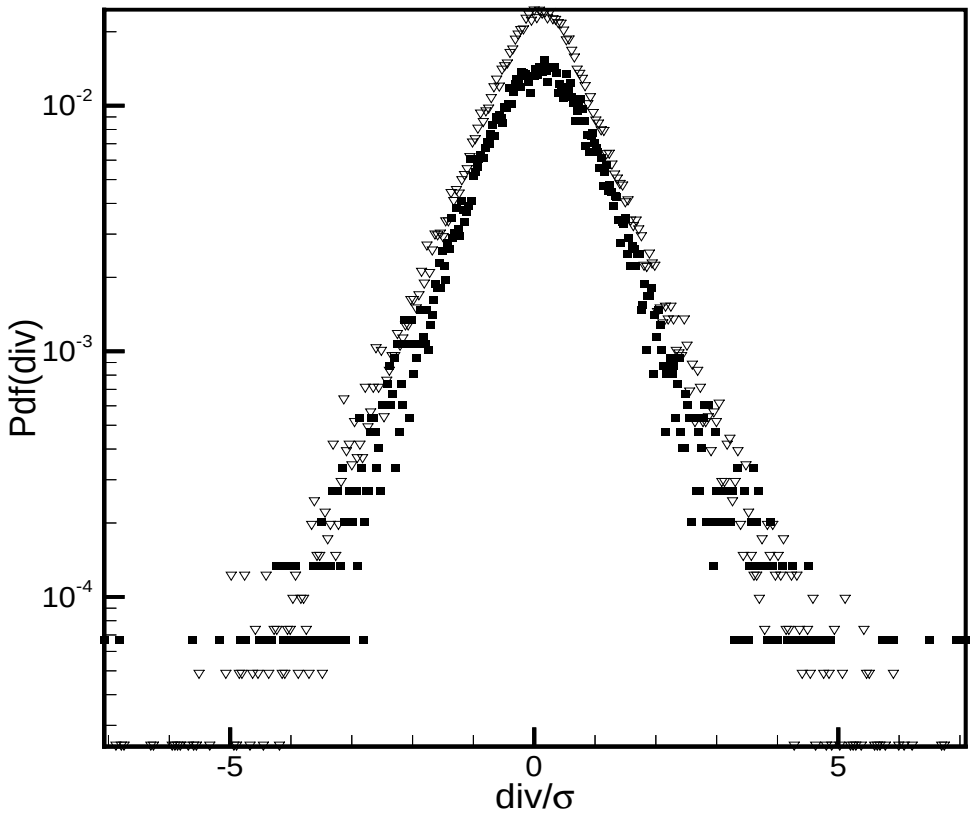

Figure 5: Probability density function (PDF) of the surface flow divergence field with $\sigma = \langle(\nabla \cdot \mathbf{v})^2\rangle^{1/2}$. $Re_\lambda = 100$ and 140, for closed and open symbols respectively.

two-dimensional divergence made on the surface. The data were extracted from an ensemble of measurements made at many instants of time and many points (x, y) in the surface. The abscissa is the divergence made dimensionless by its standard deviation. Note that the mean value of $\nabla_2 \cdot \mathbf{v}$ is close to zero and that this function has exponential tails out to almost four standard deviations, $\sigma_{\nabla_2 \cdot \mathbf{v}}$. Computer simulations of $P_{\nabla_2 \cdot \mathbf{v}}$ for isotropic forcing as well as large-scale shear likewise show this exponential behavior. Exponential behavior for the PDF can be expected, because the divergence is composed of velocity derivatives which are known to yield exponential tails in two- and three-dimensions. This result was confirmed recently by direct measurements of each of the velocity gradient components in a turbulent three dimensional flow [10]. Therefore our compressibility measurements do not distinguish the behavior of the surface flow from that in the bulk.

The compressibility on the surface is however much different from that of a plane deep in the bulk. A measure of the degree of compressibility is C, a dimensionless ratio of the average squared divergence to the average of the contraction of the full gradients, defined as

$$\mathcal{C} = \langle (\frac{\partial v_x}{\partial x})^2 + (\frac{\partial v_y}{\partial y})^2 + 2\frac{\partial v_x}{\partial x}\frac{\partial v_y}{\partial y} \rangle / \langle (\frac{\partial v_x}{\partial x})^2 + (\frac{\partial v_y}{\partial y})^2 + (\frac{\partial v_y}{\partial x})^2 + (\frac{\partial v_x}{\partial y})^2 \rangle \qquad (2.5)$$

for a two-dimensions plane(appropriate for both two- and three-dimensions.) The brackets denote an average over all points in space at several different times.

For any arbitrary plane in an isotropic three-dimensional flow one can show that $\mathcal{C}$ is fixed at 1/6[11], which is in close agreement with 0.19, the bulk results from the computer simulations. For our surface measurements the value of the dimensionless compressibility is 0.5 $\pm$ 0.1, which is again in excellent agreement with the numerical simulations. This result is achieved if one assumes that the correlation between the velocity gradients $\langle \frac{\partial v_x}{\partial y} \frac{\partial v_y}{\partial x} \rangle$ is small compared with the divergence.

The presence of the surface boundary eliminates the symmetry about the xy plane hence removing the three-dimensional isotropy responsible for the fixed value of 1/6 in the bulk.

We then turned to an investigation of the second order structure function of *longitudinal* velocity differences defined as

$$D_2(R) = \langle ([\mathbf{v}(\mathbf{x}) - \mathbf{v}(\mathbf{x} + \mathbf{R})] \cdot \mathbf{R}/R)^2 \rangle, \qquad (2.6)$$

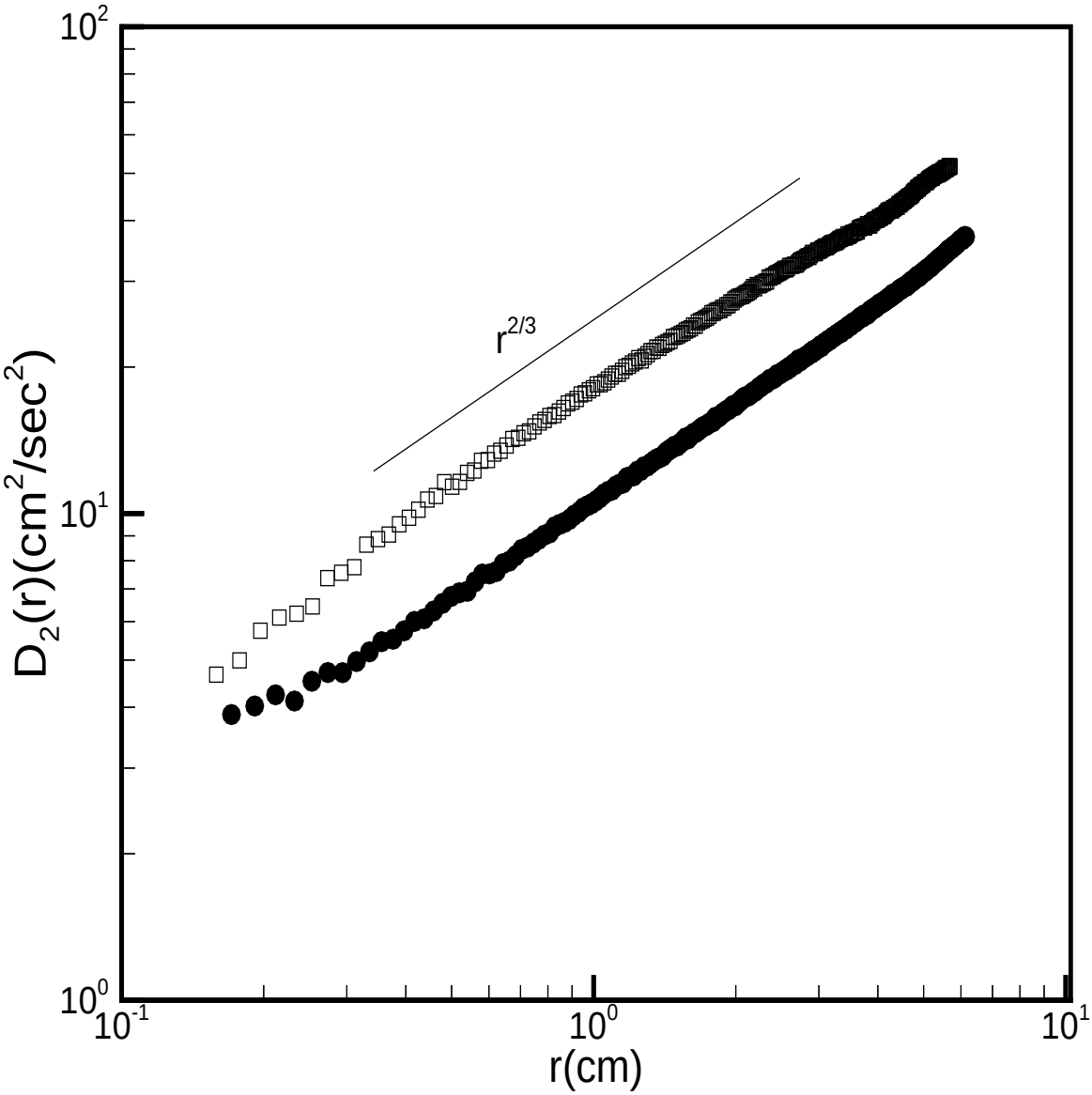

Figure 6: Second moment of the mean square longitudinal velocity difference as a function of separation r. Upper curve: 1.0 cm below the surface (Re_λ=120); lower curve: at the surface, z=0 (Re_λ=93). The solid line is the Kolmogorov prediction..

In words this is the mean square of the component of velocity differnces along the vector **r** separating the two points. The second moment provides information about the distribution of turbulent energy on different length scales. The second moment is something of a yard stick for turbulent systems. Whereas the third moment as discussed in the previous section, it is difficult to acquire sufficient statistics to produce reliable results.

The function $D_2(r)$ was measured on the surface as well as in the bulk. Figure 6 is a log-log plot of $D_2(r)$ for the surface, z=0, (lower curve) and below the surface at z=1 cm (upper curve). The Reynolds numbers Re_λ at z =0 and z = 1 cm, were 93 and 120 respectively. The dissipative scale η(see Appendix A), taken to be 0.1 mm, was too small to be resolved in these measurements. From this figure one sees that the data exhibit scaling behavior in the interval $2 \leq r \leq 60$ mm with a slope very close to 2/3 [7](the solid line in the figure), which is consistent with theoretical and experimental results for ideal three-dimensional turbulence, even though the system is compressible and capable of exchanging energy and vorticity with the bulk. Original studies revealed a very different result for $D_2(r)$[12]. The discrepancy was tracked down to an interesting form of surface contamination, which will only be discussed briefly in Appendix D.

2.5 LAGRANGIAN FLOW INVESTIGATION

Despite the obvious effects on particle dispersion evident from visual observations, the Eulerian flow measurement did not reveal any striking effect imposed on the flow structure. Therefore we focused on measurements aimed at studying the trajectories of the surface particles.

In order to investigate the time-dependent properties of the flow, measurements of the Lagrangian trajectories of an entire field of particles were made. In these measurements a time dependent velocity is assigned to an element of fluid as it moves through the laboratory frame in contrast to the above measurements where the velocity is measured at fixed points in the laboratory frame. Measurements of single particle and pair diffusion are presented,

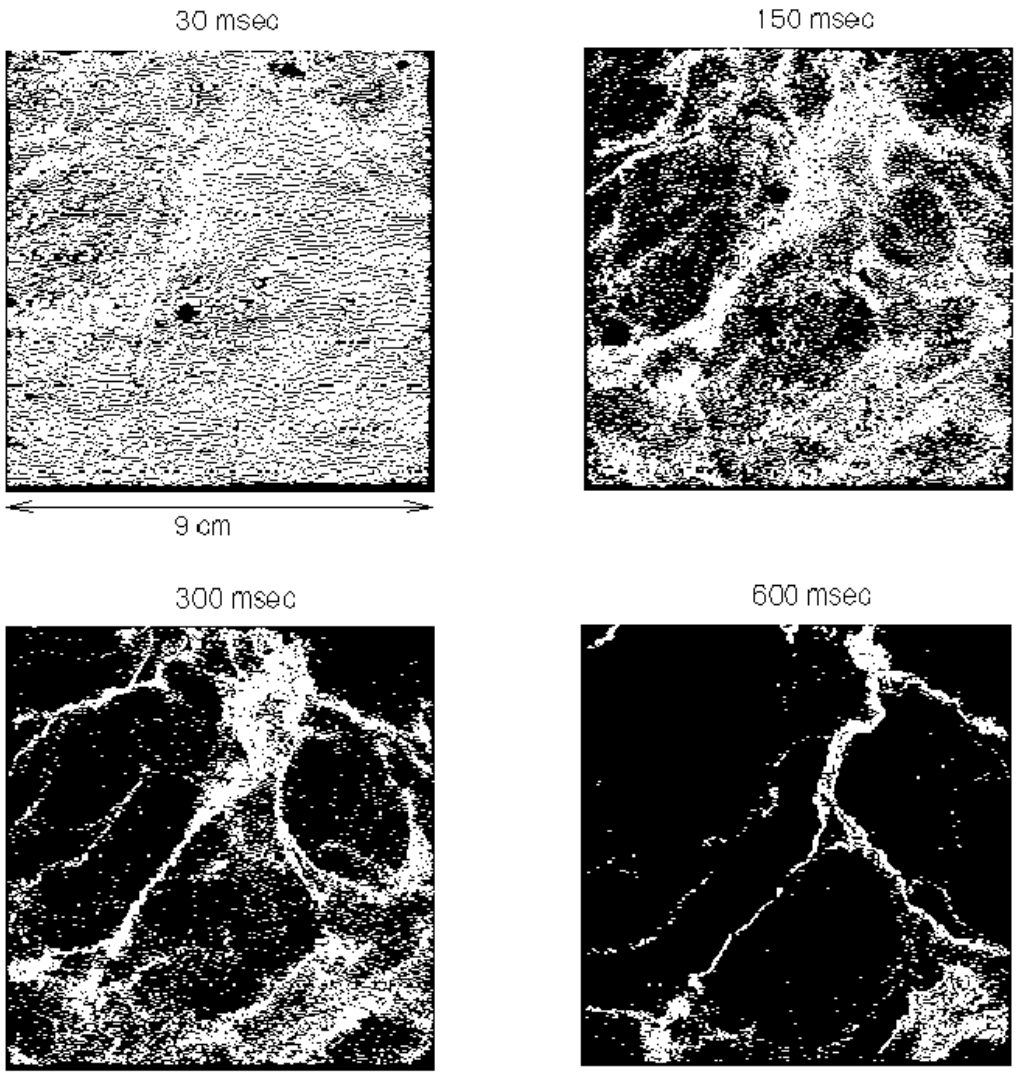

Figure 7: Series of images showing the time evolution of a field of simulated particles.

as well as multi-point measurements aimed at investigating the temporal evolution of structures in the flow. A comparison between the results from the laboratory experiment and the computer simulations will be presented in the discussion section.

The dramatic effects of compressibility on the particle field shown in Fig 1 are also apparent in the evolution of *simulated*(see Appendix B) particles tracked experimentally, as seen in Figure 7. The following dispersion results were gleaned from measurements of these particle trajectories.

2.5.1 Single particle diffusion

By tracking an ensemble of particles one is able to establish a typical distance and time that a particle travels before its motion becomes uncorrelated. Figure 8 is a plot of the single-particle diffusion, $d^2(t) = \langle [x(t) - x(0)]^2 \rangle$. Here, and for all Lagrangian measurements, the brackets denote an average over all particle tracks in a given sequence of images as well as an ensemble of sequences. The average distance that the particles travel over the first time step is larger then the dissipative scale, η. Therefore these measurements only probe the action of the velocity field in the inertial range.

Very strong projectile-like motion, $d^2(t) \propto t$, is seen in the initial interval $0.4 < d < 9$ mm. This scaling persists for a decade beyond the estimated viscous subrange η=0.1 mm. The abscissa is normalized by the Kolmogorov time τ_η, which is found experimentally to be no longer than 1/80 sec. Fully ballistic motion in the inertial range suggests that a particle's lagrangian velocity is highly correlated, i.e. the lagrangian correlation time $\tau_\mathcal{L}$, is quite long. Two different time scales can be used to approximate the temporal correlation for a fluid element. In the Eulerian frame one uses the eddy turnover time (see Appendix A) at the largest correlated scale l_0. The eddy turnover time τ_{l_0} is approximately 80 τ_η. In the Lagrangian frame the temporal correlation function for a fluid element is used(see appendix A.)the Lagrangian correlation time, $\tau_\mathcal{L}$ for this experiment turns out to be of the same order of magnitude as τ_{l_0}.

The slope decreases smoothly out to $d \simeq 50$ mm and $t/\tau_\eta \simeq 100$, where the motion becomes uncorrelated, that is $d^2(t) \propto t$(a better fit to the data is a line of slope 0.9 shown in the figure).

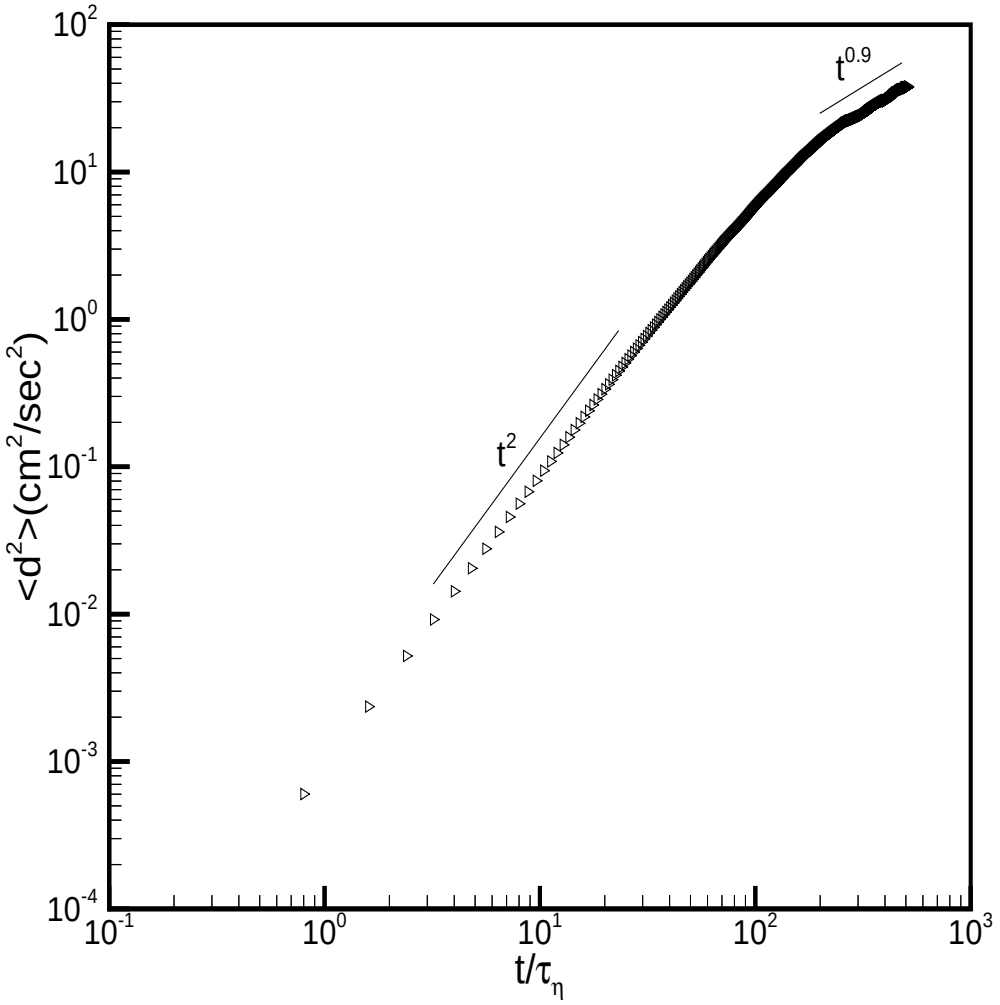

Figure 8: Single-particle diffusion on the surface. The solid lines have slopes corresponding to ballistic motion (slope = 2) and, at large d, the slope is close to Brownian, which is unity. This data was extracted from an ensemble of runs where $Re_\lambda \simeq 100$.

At this time and displacement the particles are experiencing Brownian motion. Similar results were found for the tracer particles in the computer simulations. These observations are in accord with the expected result for incompressible turbulence [13]. Therefore the high compressibility does not seem to effect the statistical behavior of single particle diffusion.

2.5.2 Richardson diffusion

By measuring the evolution of the separation, $\langle \Delta^2(t) \rangle$, of particle pairs it is possible to investigate the flow's dispersive nature. This measure gives limited insight into the manner in which the flow field changes in time. As already discussed, for ideal turbulence one expects that the separation of particle pairs should grow as t^3. Here we find that although scaling does exist, it is much less than that which is found in an ideal flow.

Figure 9 is a plot of $\langle \Delta^2(t) \rangle$, where all particle pairs were initially separated by 3 mm. The thin line of slope 1.7 fits our data rather well for over a decade of Δ. We lack a full understanding of why this slope is roughly half of the expected value of $\alpha = 3$, but it certainly must be connected with the strong compressibility at the surface and the persistent ribbon like structures it produces.

Measurements of $\Delta^2(t)$ were averaged over 27 runs. In each run roughly a thousand simulated particle pairs were tracked for up to 10 s at a data collection rate of 100 Hz. In the individual runs, the slope varied between 1.6 and 1.9, with the average being 1.7 and the standard deviation $\sigma = 0.1$. The largest measured pair separation was 20 mm, still within the integral scale $l_0 \simeq 30$ mm, which explains why random Brownian diffusion $\Delta^2(t) \propto t$ is not seen. Particle trapping and the finite area of measurement prevent tracking particle separations to even larger values of Δ.

Here, for the first time, we see significant effects on the flow structure due to the compressibility.

2.5.3 Geometric structures

It is possible to extract, in a statistical sense, the effects of turbulence on objects of a given shape and volume by following several points simultaneously. In this way one can ascertain,

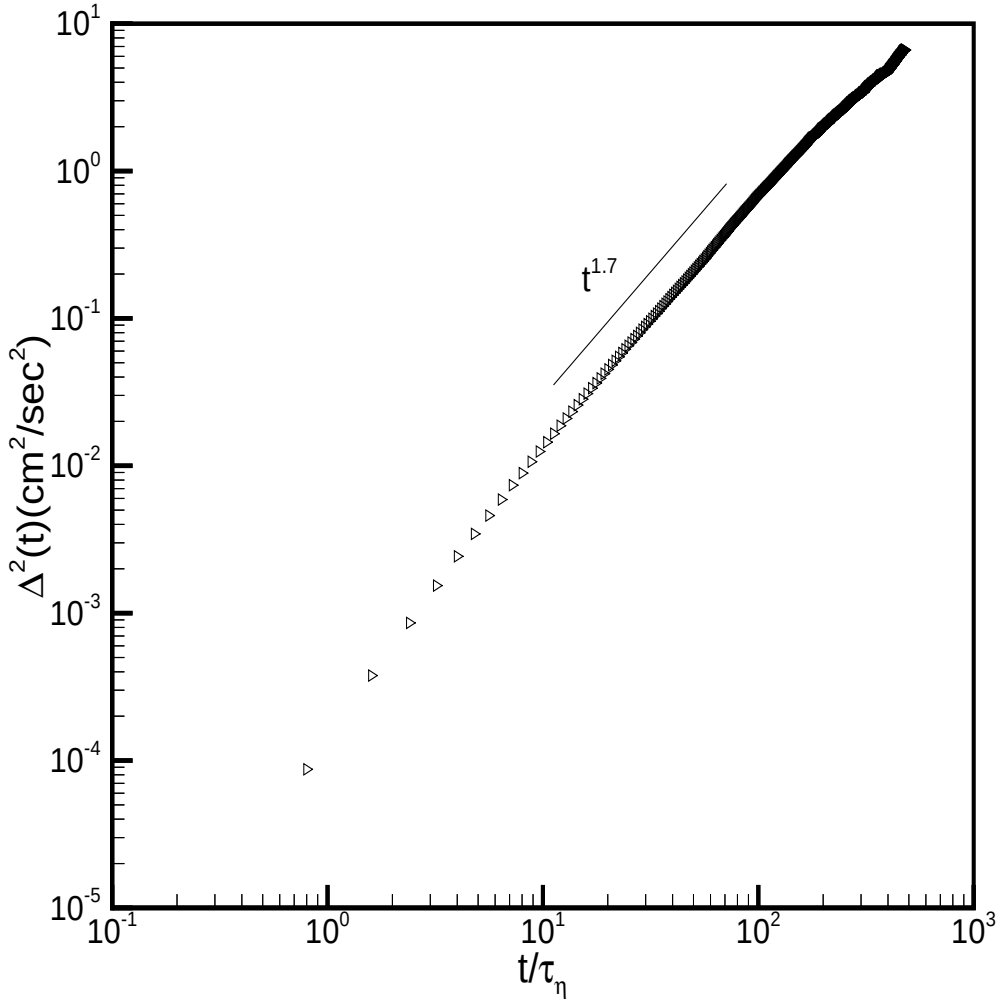

Figure 9: Growth of the mean square displacement of particles pairs. The initial particle separation is $\Delta(0) = 3$ mm. This data was extracted from an ensemble of runs where $Re_\lambda \simeq 100$.

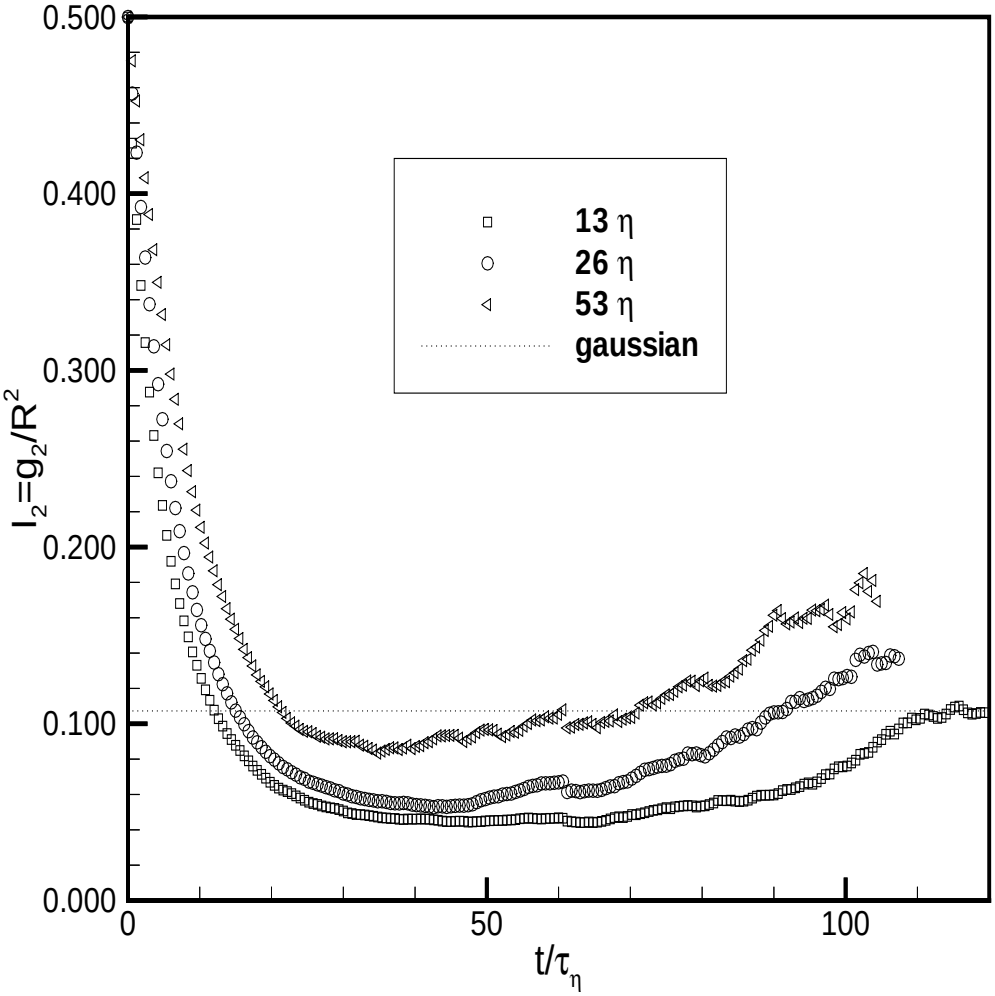

Figure 10: Temporal evolution of $\langle I_2 \rangle$ at $Re_\lambda = 100$. The runs are for triangles with different initial side lengths as indicated in the legend.

on average, the full spatial structure of the flow and its temporal evolution. In three-dimensions, where three points define a plane, four points are needed to investigate the total action of the flow including rotation, contraction and expansion in all directions. In other words, in order to probe spatiotemporal structure of the full velocity field both perpendicular to the plane and in the plane of the first three points a fourth particle is needed. This method also provides information about the mechanisms responsible for particle advection at different time and length scales in the Lagrangian frame.

In two-dimensions only three points are needed to measure all of the effects of the flow. The evolution of shapes formed by three particles tracked simultaneously thus captures the statistical behavior of the flow[14, 15]. By neglecting the center of mass, the relative position of three points can be conveniently expressed by the following two vectors, $\mathbf{a}_1 = (\mathbf{x}_1 - \mathbf{x}_2)/\sqrt{2}$ and $\mathbf{a}_2 = (2\mathbf{x}_3 - \mathbf{x}_1 - \mathbf{x}_2)/\sqrt{6}$ [15]. The distortion of a triangle is measured by the ratio $I_2 = g_2/R^2$ which relates its radius of gyration, $R = \sqrt{a_1^2 + a_2^2}$, to the smaller half-axis, g_2, of the smallest ellipse that covers the tracer triangle. From [15] one can write for two-dimensions

$$I_2 = \frac{1}{2}\left[1 - \sqrt{1 - \frac{4}{R^4}(\mathbf{a}_1 \times \mathbf{a}_2)^2}\right] . \tag{2.7}$$

Measurements of the evolution of $\langle I_2 \rangle$ are presented as a function of time and we propose a qualitative explanation based on the high compressibility in this system.

Measurements of I_2 are shown in Fig. 10. The particles were initially placed to form equilateral triangles, for which $I_2 = 1/2$ (i.e. $\mathbf{a}_1 \perp \mathbf{a}_2$ and $|\mathbf{a}_1| = |\mathbf{a}_2|$). The three curves are for triangles of different initial side length.

Pumir et *al.* [14] argue that coherent shear is responsible for flattening initially equilateral triangles, causing a decrease in $\langle I_2 \rangle$. After a sufficiently long time, random small-scale fluctuations tend to drive $\langle I_2 \rangle$ towards an equilibrium value. The equilibrium value is determined by assuming the distribution for the vectors $\mathbf{a_1}$ and $\mathbf{a_2}$ is Gaussian with zero mean and a variance determined from the average radius of gyration (for a detailed derivation please refer to [15]). The equilibrium value is $I_{2G} = (1 - \pi/4)/2$. In the two-dimensional incompressible case experiments show that the Gaussian limit is achieved in roughly 20 t/τ_η [15]. It was asserted in Ref. 18 that coherent shear should dominate in the viscous subrange and give way to the randomizing effects of turbulent mixing at larger scales.

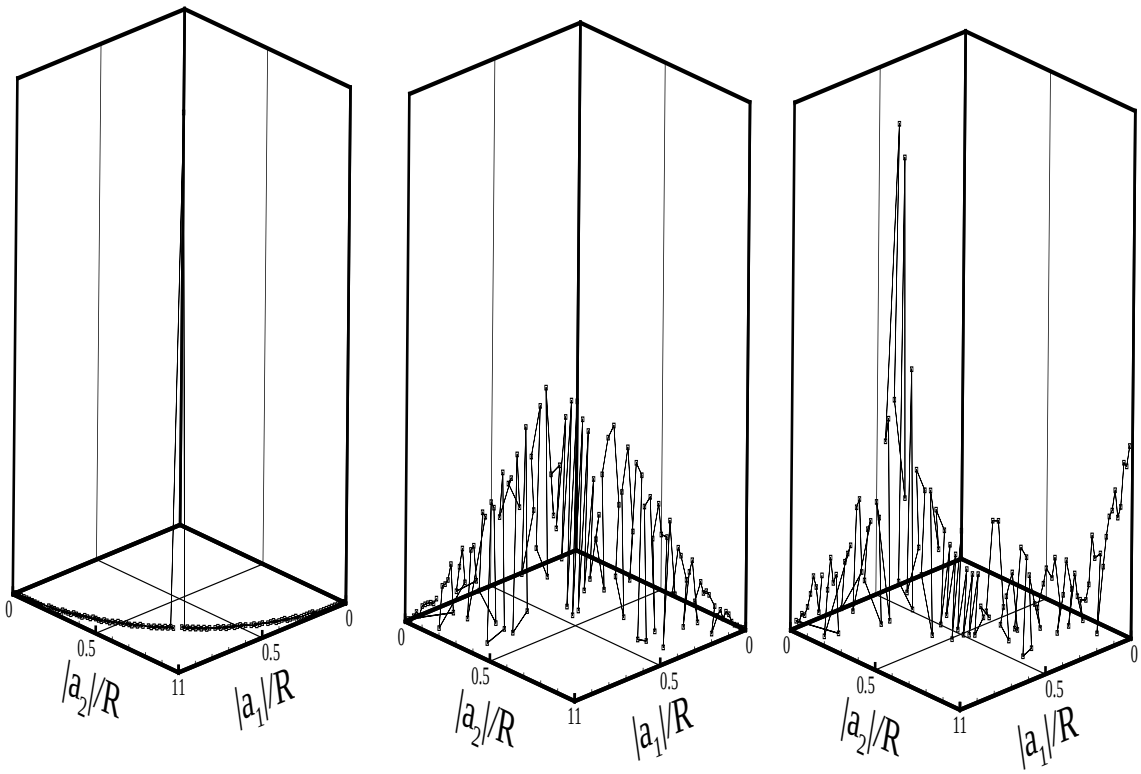

Figure 11: Joint probability distribution functions of the vector magnitudes a_1 and a_2. The far left frame was taken at t=0, where the distribution is singular at $|a_1|/R = |a_2|/R = 1/\sqrt{2}$. The middle frame is at .113 sec(9 t/τ_η) and the right frame was taken at 1.13 sec (90 t/τ_η). The initial side length was 13η, and $Re_\lambda \simeq 100$.

The measurements in Fig. 10 show a strong dip below the asymptotic value of I_{2G} and an extended minimum that exists for triangles initially having a radius of gyration significantly larger than the dissipative scale. This behavior can be accounted for by strong clustering that is apparent in Fig. 1. The triplets are quickly compressed into quasi-colinear configurations, making $\mathbf{a}_1$ almost parallel to $\mathbf{a}_2$ forcing I_2, shown in Fig. 10, towards zero (see Eq. (2.7)). In incompressible turbulence, this effect is absent, and I_2 very soon attains its random Gaussian value I_{2G}. The data attain a value of I_2 that is slightly larger than the Gaussian value. Significantly longer runs would be required to check whether the Gaussian value is the asymptotic limit for this experimental realization.

In order to further probe the behavior of the particle triplets the joint probability distributions of $|a_1|/R$ and $|a_2|/R$ have been measured. The results are shown in figure 11. Initially the distribution is a spike at $|a_1|/R = |a_2|/R = \sqrt{2}/2$. After a short time the distribution spreads out indicating that the triangles are becoming highly distorted. The most interesting effect occurs at longer times when two maxima begin to appear, when $|a_1| \gg |a_2|$ and $|a_2| \gg |a_1|$.

The above results suggest that the compressibility is acting to flatten triangles, even when R is much greater than η, contrary to incompressible flows [14]. A dominant number of triangles remain distorted for very long times.

2.6 DISCUSSION

As already stated, the Eulerian measurements as well as single particle diffusion are in accord with the excepted results for ideal Kolmogorov behavior. The simulations of Schumacher and Eckhardt are also in agreement with this result. Here we focus on Richardson, or pair diffusion. Scaling close to the Richardson prediction was found in experiments [16] as well as in high-resolution numerical simulations [17] carried out in the inverse cascade of two-dimensional incompressible turbulence.

There are several possible reasons why the value of α is smaller then expected. Firstly is the presence of intermittency, which tends to decrease the scaling exponent for the structure

functions. Intermittency is the presence of large fluctuations in the turbulent velocity associated with the phenomena of vortex stretching(see appendix A.) However, intermittency effects, if present, seem to modify this exponent only slightly [18].

A second mechanism that could be responsible for the reduction in the scaling exponent α is the action of waves. Although the apparatus was designed to minimize surface waves, it is impossible to completely eliminate them. An Hamiltonian model successfully accounts for the motion of particles floating on a container of vertically oscillating fluid where capillary waves are excited [19, 20]. This theory is valid for systems where the vorticity, or curl of the velocity field, is small enough to be neglected. In order to test the validity of this theory we measured the surface vorticity, of magnitude $\omega(x, y)$. Measurements of the (vertically directed) vorticity of the surface particles show that it is quite large. The second moment of the surface vorticity,

$$D_\omega(r) = \langle([\omega(\mathbf{x}) - \omega(\mathbf{x}+\mathbf{r})])^2\rangle = 2 * (\langle\omega^2\rangle - \langle\omega(\mathbf{x})\omega(\mathbf{x}+\mathbf{r})\rangle) \tag{2.8}$$

saturates at a rather small value of r, and approaches the limiting value $2\langle\omega^2\rangle$. A dimensionless measure (Q) of the surface vorticity is $D_\omega(r)r^2/D_2(r)$, which relates the amount of rotational energy to the total kinetic energy. At r equal to the outer scale of the turbulence, $l_0 \simeq 3$ cm,Q $\simeq 1$, which suggests that it is probably too large to satisfy the zero-vorticity requirement of wave turbulence theory. This observation is in agreement with measurements that show $D_2(r)$ is insensitive to wave amplitude.

One may argue that the reduced diffusion is due to the fact that the surface flow does not adhere to the assumptions used in the Kolmogorov derivation. The underlying fluid can exchange kinetic energy with the water molecules below. Making $\epsilon(cm^2/sec^3)$ the flow of energy density an ill-defined quantity. Energy is exchanged very abruptly wherever the bulk flow impinges on the surface, or recedes from it due to the constraint of the surface. Hence, the energy of the floaters still would not be constants of the motion, even if the underlying fluid were inviscid and undriven. With the above conservation laws absent, one lacks the traditional dimensional arguments to estimate the scaling forms of the velocity structure functions. However the second moment, $D_2(r)$, is in good agreement with ideal flow.

Here it is proposed that the system's strong compressibility is responsible for the decrease in the scaling exponent α. The effects of compressibility on turbulent diffusion has recently come under theoretical scrutiny [21]. Modelling the flow as Gaussian with negligible temporal correlation, one can show that a uniform distribution of particles will coagulate if the dimensionless compressibility, $\mathcal{C}$, exceeds a critical value $\mathcal{C}_c$, which for the geometry of this experiment is 1/2 [13]. Although, assumptions contained in this model make it inapplicable to laboratory experiments it is interesting to note that the measured value of $\mathcal{C}$ is very close to this critical value.

Since an applicable theory for compressible motion has yet to be developed, we again turned to computer simulations for comparison, and guidance[5], which were in remarkably good agreement with the first reported observations [12, 22]. Whereas the computer simulations (see appendix D) were able to probe particle pair separations at arbitrarily small distances, limitations in computational time will only permit the investigation of a relatively small inertial range. The computer model measures a scaling exponent for pair diffusion close to the measured value for the inertial range measured in experiment. The computer simulations also show a very short Richardson-like scaling just beyond the viscous sub range. These scales are immeasurable in the laboratory experiment.

It has been proposed [23] that the almost ballistic scaling, with $\alpha = 2$ is due to the highly correlated motion of particles trapped in the thin ribbons. Random diffusion-like motion in more clustered regions acts to reduce the exponent below 2. In other words large portions of the initial distribution of particles are forced through bursting and subduction into narrow veins and clumps at vertices.

We now turn to the measurement of particle triplets. Again, although there are theoretical predictions[14] for the evolution of triangles for ideal flow, the simulations provided the most capable comparison. For short times the qualitative behavior for the triangles in both the experiments and computer simulations are in good agreement. However,the triangles in the computer simulations (not shown here) show an even stronger tendency to remain flat and appear to approach an equilibrium value smaller than I_{2G}. Self-avoidance of the finite-size particles and possibly the particle tracking resolution used in the laboratory experiments force a limit on the minimum attainable value of $\langle I_2 \rangle$ and cause this quantity to increase at

later times. In the numerical study (point) particles can become arbitrarily close and thus $\langle I_2 \rangle$ can remain at a small value well below Gaussian.

A similar effect is illuminated in a comparison between the pdfs shown in figure 11 and their analogs in the computer simulations. Whereas similar behavior is seen in the simulations, the maximum at $|a_1| \simeq 0$ is much more pronounced for the simulations. This again reflects the fact that the point particles used in the simulations are capable of attaining much smaller separations than in the experiments. Most of the discrepancies are do to the limited inertial range of the computer simulations, and the finite particle size in experiments.

2.7 CONCLUSIONS

The effect of compressibility, which is probably best revealed by measuring statistics of the particle surface density, as in Fig. 1, should also be apparent in structure of the velocity field as revealed in the structure functions $D_n(r)$ and the time variation of particle pair separations $\langle R^2(t) \rangle$. Our laboratory experiments and the computer simulations of Eckhardt and Schumacher show that $D_2(r)$ scales as in 3D turbulence, but the computer simulations show that higher moments of velocity differences display stronger intermittency than in 3D turbulence. This effect has yet to be verified in the laboratory.

As for pair diffusion, self-similarity is seen over a wide range of separations, but the exponent α in the expression $\langle \Delta^2(t) \rangle \propto t^\alpha$ is much smaller than the Richardson result, $\alpha = 3$. One might expect that large compressibility would diminish α, which is consistent with the experimental result, $\alpha \simeq 1.7$, for measurements where R is in the inertial range (For R much larger than the integral scale of the turbulence, $l_0 \simeq 3$ cm, the relative motion the particles should be random, making α =1).

The relative motion of passive tracer particles in our *compressible* flow is very different from tracer motion in incompressible turbulence. The turbulence creates locally convergent and divergent regions of particle density, inhibiting dispersion. This difference is intimately related with the fact that the Kolmogorov-Richardson pair dispersion prediction ($\langle \Delta^2(t) \propto t^3$) is not realized in the motion of the floating particles. Likewise, the evolution of geometrical

structures, revealed in the motion of particle triplets strongly differs from incompressible fluids.

One wonders if the results presented here should be identical to observations of relative dispersion in a turbulent fluid at high Mach number where $\nabla \cdot \mathbf{v}$ can likewise be large. For the floaters there must, of necessity, be ripples on the water surface, however small their amplitude, and these relieve sharp pressure changes which could be considered as a kind of precursor of small scale shocks for supersonic flows. Thus one might expect that some of the features observable in these low Mach number experiments should also be observable in supersonic flows.

In summary, the presence of high compression, greatly alters the structure of the flow. The inability of the flow to support strong saddle-like structure reduces the degree to which the turbulence can separate particle pairs.

2.7.1 Further studies

As previously mentioned, the best way to study the effects of incompressibility may be by measuring the statistics of the density field of particles on the surface $\theta(x, y, t)$. Measurements will include multi-fractal analysis of surface structures as well as spatial correlations of the density field.

To a good approximation the magnitude of $\theta(x, y, t)$ does not effect the velocity field, making it a passive scalar field. The equation governing the evolution of $\theta(x, y, t)$ is linear as shown below and, hence it is more tractable than the Navier-stokes equation. $\partial\theta/\partial t + \mathbf{u} \cdot \nabla\theta = \kappa\nabla^2\theta$ However it has been shown that the multi-point measurements, such as density-density spatial correlation functions, exhibit intermittent behavior even when the velocity field does not[24]. This system may be an excellent tool for investigating the nature of intermittency.

3.0 MODIFICATION OF A VORTEX STREET BY A POLYMER ADDITIVE

3.1 INTRODUCTION

It has long been known that the drag force exerted by a fluid flowing in a pipe is markedly larger if the fluid is turbulent rather than laminar.[25] Some 50 years ago it was discovered that the addition of a very small amount of a long chain polymer to the turbulent fluid has the effect of suppressing this excess drag.[26] This phenomenon is still not understood. While large on an atomic scale, the polymer molecules are much smaller than the smallest eddy sizes one expects to find in the turbulent fluid, at least when the molecules are in their relaxed coiled-up state. The problem is doubly complex because it involves two imperfectly understood subjects, i.e., the rheology of the molecules when they are exposed to shear and the phenomenon of turbulence itself.

The present experiment was undertaken to reduce the complexity of the problem by examining the effect of a polymer additive on a flow that is only weakly turbulent[27]. The phenomenon being studied here is the influence of the polymer additive on vortex shedding in a quasi-two-dimensional system, namely a rapidly flowing soap film, through which a rod has been thrust. At the onset of vortex shedding, the turbulence is very weak in the sense that it can be described by a language appropriate to nonlinear systems in which relatively few degrees of freedom are excited.[28, 29] Drag reduction by a polymer additive in this simple type of flow has been studied for many years.[30, 31, 32] One might hope that drag reduction and the suppression of turbulence in the bulk fluid are manifestations of the same phenomenon. However, a definitive experiment by Cadot et al.[33] shows that this hope is not realized. While it is observed that the polymer additive suppresses small-scale velocity

fluctuations in the turbulence[33, 34] far from the container walls, drag reduction is due to the alteration of the shear layer near the boundaries.

The experiment reported here probes the effect of the polymer polyethylene oxide(PEO) on a boundary layer. Vortex shedding, with which we are concerned here, refers to the generation of pairs of vortices by a cylindrical rod in a water tunnel or wind tunnel where the flow is otherwise uniform.[35] Boundary layer separation occurs at a moderate mean flow velocity U_f and leads to the creation of recirculating vortices. The vortices remain attached to the rod due to a balancing of shear and pressure forces. As U_f is increased, a shear instability behind the vortices causes the flow to become periodic. When a critical value of U_f is reached, the flow becomes unstable, causing the vortices to detach from the rod. The vortices that peel off the rod are in the form of staggered, counter-rotating pairs that are convected downstream.

In our soap film measurements, laser Doppler velocimetry (LDV) was used to measure the local velocity at various points below the rod. The vortex street produced by this rod can also be observed by eye because the vortices give rise to variations in the film thickness, which has an average value of a few micrometers. The thickness variations $\delta h(x, y, t)$ produce an interference pattern which is displayed in Fig. 12. The flow, which is downward in the experiment, is from left to right in the figure. The rod, which is perpendicular to the film, may be seen at the left. The mean vertical flow speed is 1.7 m/s. The polymer concentration is 0 in Fig. 1(a) and 30 wppm in Fig. 1(b). The molecular weight of the polymer used in most of these experiments is $M = 5X10^6$.

In spite of its low concentration, the polymer additive strongly disorders the regularly shed vortices seen in Fig. 1(a). A discussion of these figures is deferred to Sec. 3.4.

A measurement of the time dependence of $v_y(t)$, the component of velocity perpendicular to the flow direction, is strongly sinusoidal.[28, 36] The power spectrum, $S(f)$, of $v_y(t)$ is sharply peaked at the shedding frequency, $f = f_s$.

One effect of the polymer is its reduction of the kinetic energy contained in the velocity fluctuations. The measurements show that the polymer also lengthens the boundary layer behind the rod.[25] We believe this stretching effect arises from the enhancement of the elongational viscosity, which is appreciable even at such low polymer concentrations, provided

the molecular weight is high. The elongational viscosity is known to depend strongly on the molecular weight of the polymer. The present experiments show that a polymer additive of molecular weight $5X10^6$ strongly alters vortex shedding, whereas a polymer of much higher concentration but having a molecular weight of $3X10^5$ has no effect. This observation gives further credence to the idea that the elongational viscosity is implicated in the effects that are seen. The high molecular weight polymer also broadens the otherwise sharp frequency power spectrum $S(f)$.

The strong effect of a polymer additive on vortex shedding has recently been seen in a vertical water channel.[37] In that experiment a polymer solution of relatively high concentration was injected into the flow through the holes in the cylinder that generate the vortex street. A dye in the injected solution showed that the polymer alters the lateral spacing of the chain of counter-rotating vortices and produces other visible effects as well. Details of our experiment are presented in the next section and the results are given in 3.3. The fourth section is a discussion of our findings, and the work is summarized in the final section.

3.2 EXPERIMENT

The sheet of flowing soap film is formed between a pair of thin nylon lines suspended vertically and held taut by a weight at the bottom.[38] The separation, W, of these lines, is 5 cm, and the height of the channel is roughly 2 m. The mean film thickness h is in the range $2 \leq h \leq 5\mu$m. At the top of the soap film tunnel is a reservoir of soap solution which is fed through a valve to the vertex where the wires join. The mean flow speed is adjustable in the range 0.5 m/s $\leq U_f \leq$ 2.5 m/s.

The spent soap solution is collected in a second reservoir at the bottom. The polymer-containing solution was not recirculated back to the top reservoir with a pump to avoid rupturing the polymer chains as the solution flows through the pump.

In most vortex shedding experiments the control parameter is the Reynolds number, defined as Re $= U_f d/\nu$, where ν is the kinematic viscosity of the flowing medium. In a soap film experiment, ν is a function of the thickness and is therefore not equal to the viscosity of the

bulk mixture. Rather, it has contributions from the surfactant layers on the film surfaces and the solution in the interior, which is mainly water.[37, 39, 40, 41, 42, 43]

The onset of vortex shedding in these soap films appears at $U_f \simeq 0.5$ m/s.[44] In three-dimensional flows this onset corresponds to $\mathrm{Re} = \mathrm{Re}_c = 47$.[28, 29] The present measurements were made at $U_f \simeq 2$ m/s. In our soap films this corresponds to a Reynolds number of roughly 400.

In this experiment the rod was made of glass, its diameter d being fixed at 2 mm in all the experiments. A clean glass rod is wetted by the soap solution, causing the film thickness to increase in an annular region that extends radially for a fraction of a millimeter. This local thickness increase is roughly a micrometer. The same visual vortex street pattern seen in Fig. 12(a) is generated even when the rod is made of a nonwetting material such as teflon.

The mean vertical flow speed of the soap films varies measurably with the distance from the upper vertex. For approximately the top third of the channel height the film is accelerating, and for the bottom third it is decelerating. All measurements were therefore made in the central third of the channel. The addition of the polymer did not have an appreciable effect on the vertical variation of the mean flow speed.

The desired concentration of the PEO solutions was achieved in two successive dilutions, as described elsewhere.[34] Care was taken to ensure that the polymer additive had ample time to fully dissolve in the neat 1 percent soap solution, the detergent being Dawn.[45] Measurements were taken using a two-probe TSI laser Doppler velocimeter. With one of the probes, U_f was measured 5 cm above the rod. The film was seeded with polystyrene latex particles having a diameter $d = 1\mu$m, their concentration being $\sim$50 μl per liter of soap solution. At this concentration the counting rate was maximized.

A fast Fourier transform (FFT) program was used to extract the power spectra $S(f)$ from the velocity record $v_y(t)$. Because the seed particles pass through the observation point at irregularly spaced intervals, a standard binning procedure is used to obtain a record of velocity at equally spaced time intervals. The spectra were determined from a set of 200 000 points, which required making measurements for several minutes. Each run was broken into several 2048 point segments for averaging, and hanning windows were used to reduce leakage effects.

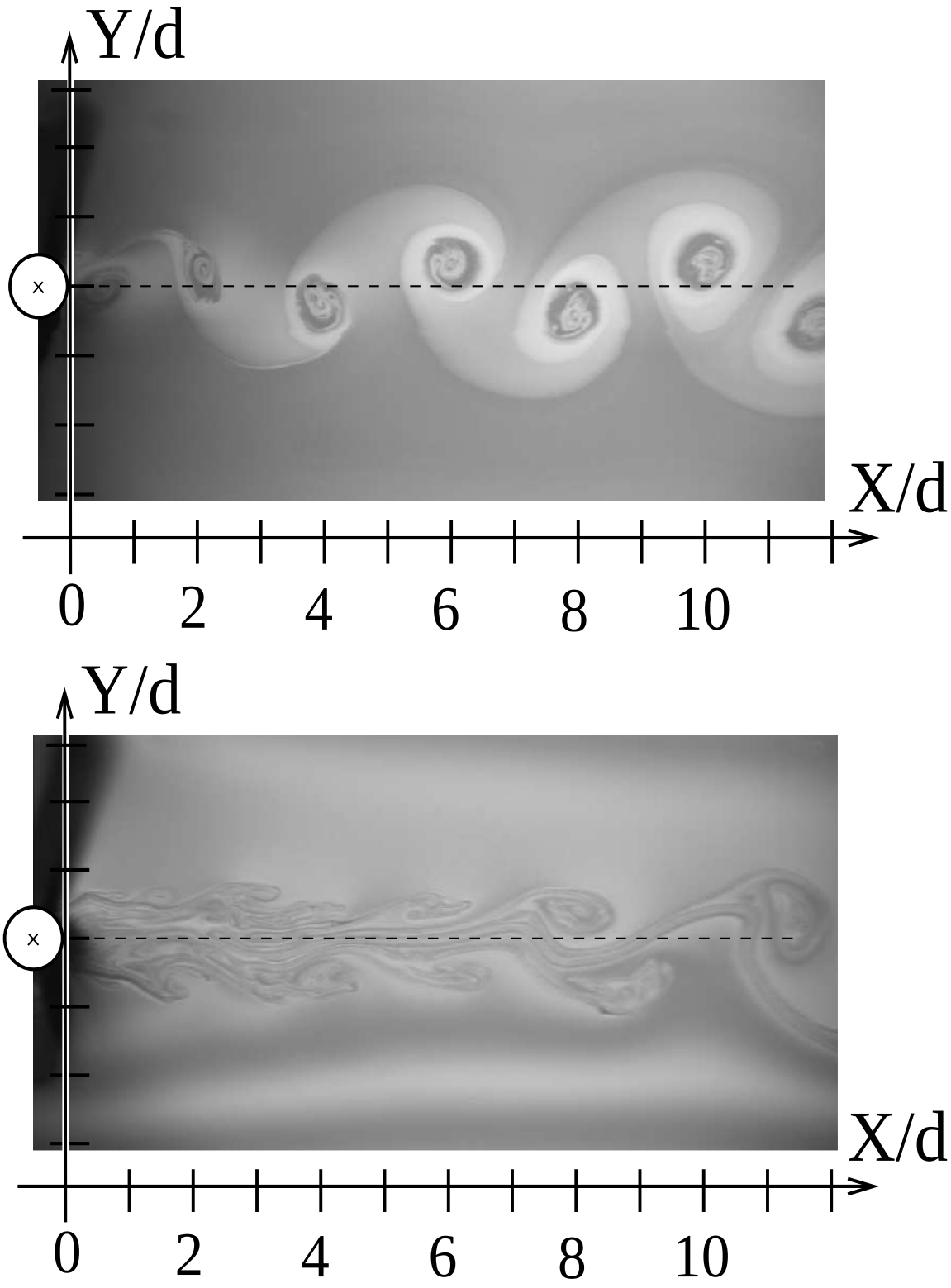

Figure 12: Images (a) and (b), respectively, show the vortex street in a polymer-free film and in a film where the polymer concentration is 30 wppm molecular weight M is $5X10^6$).

The viscosity η of the bulk soap-water-polymer solutions was measured in a Brookfield[46] viscometer operating at 4 Hz. As the polymer concentration was increased from 0 to 200 wppm, η increased from 1.1 to 1.4 cp. When glycerol is added to the mixtures to ensure that all the measurements were made at the same value of η, the recorded spectra were the same as the $S(f)$ measured with the glycerol absent. Therefore glycerol was never added to the solution.

3.3 RESULTS

The dominant effect of the polymer can be understood from Figs. 13 and 14. Shown are the time-averaged longitudinal and transverse velocities $U((X,Y))$ and $V((X,Y))$, respectively. Here X is the downstream distance below the bottom of the rod and Y is the transverse coordinate, with $Y = 0$ at the rod axis. These figures display the effects of the polymer on the time-averaged velocities as functions of X and Y. The time-averaged transverse velocity along the center of the rod remains zero at all points below the rod. For this reason these data are not presented.

Figure 13 is a semi-log plot of the normalized longitudinal velocity U/U_f as a function of X/d keeping $Y = 0$. The curves in this figure show data for the polymer-free soap film and for soap solutions containing 30 wppm of PEO. Measurements for concentrations of 0 and 30 wppm are denoted by closed and open circles, respectively, in all figures presented here. The dashed and solid lines are a guide to the eye. The velocities will be designated by the subscripts 0 and 30 for $c = 0$ and $c = 30$ wppm.

From Fig. 13 it is seen that $U_0(X)$ is negative for $0.1 \leq X/d \leq 0.8$. The negative sign is indicative of the presence of the vortices before they detach from the rod. For greater values of X/d, $U_0(X)$ rises, reaching a (local) maximum at $X/d \simeq 3$, before rising toward the mean flow velocity far downstream. In contrast, U_{30} for the polymer-doped solution remains negative out to $X/d \simeq 3$ and then slowly increases monotonically toward the mean flow velocity $U_{30} \simeq U_f$. At $X = 0$, U must become 0, but a slight horizontal misplacement of the velocity probe prevents this limit from being reached.

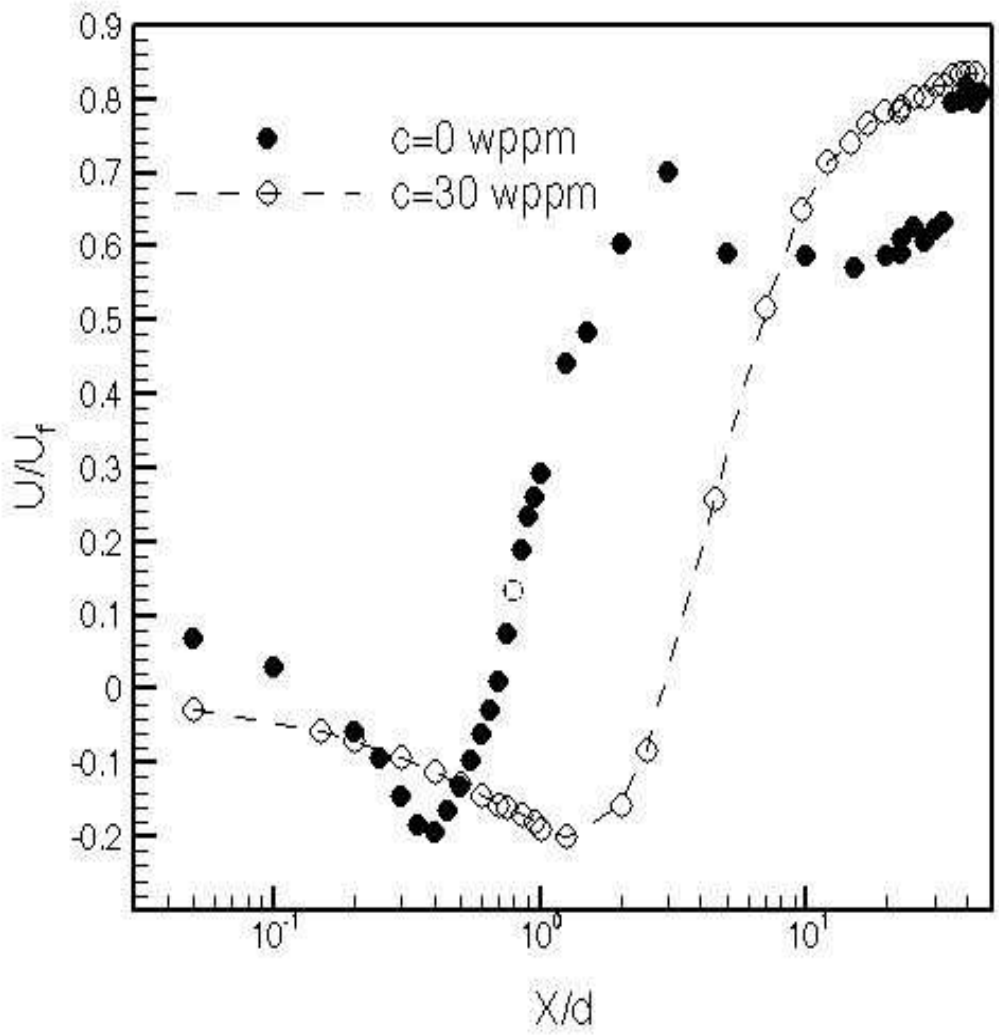

Figure 13: Time-averaged longitudinal velocity measured directly below the rod vs the downstream distance. The open and closed circles show data for the polymer-free and polymer-containing films. The ordinate and abscissa are expressed in dimensionless units, with U_f the mean vertical flow speed well above the rod.

The two curves in Fig. 13 appear to be of the same form, aside from a stretching of the abscissa in the polymeric flow. We can explain this stretching by assuming that the polymer alters the elongational viscosity of the fluid. The elongational viscosity η_{el} is defined by $N_1 = \tau_{xx} - \tau_{yy} = \eta_{el}\partial u/\partial x$, where the left and right sides are time averages over very many vortex shedding periods. Here N_1 is the first normal stress difference or the non-shear force exerted by the fluid[47].

A measurement of the flow rate, A, of the soap film through the channel with the polymer present and absent showed that the polymer reduces A by less than 15 percent. This result indicates that the change in N_1 due to the polymer additive is very small in comparison to the dramatic reduction in the longitudinal velocity gradient. If this change in N_1 can be neglected, we can estimate the change in η_{el} by noting the shift in the minima in Fig. 13. From these measurements the increase in elongational viscosity due to the polymer is seen to be roughly a factor of 5.

The polymer also alters the Y-dependence of the velocity field $V(Y)$ shown in Fig. 14. This velocity profile is plotted at a point where the difference in behavior of the two solutions is clearly apparent, namely $X/d = 1$. The effects of the polymer weaken at positions downstream, as will be seen in data presented below. For the polymer-free vortex street, $V(Y)$ is seen to have a minimum at a value of Y roughly equal to half a rod diameter (by symmetry this velocity component will go through a positive maximum at a negative value of Y). The fact that $V(Y)$ is negative for $Y < 0$ and must be positive for $Y > 0$ establishes that the flow is converging to the center line, as expected. For the polymer-containing solution, $V \simeq 0$ for an extended range of Y at this distance behind the rod. This indicates that the flow is not converging this close to the rod. These measurements are consistent with the data in Fig. 13, which show that the formation length of the vortices has been lengthened by the presence of the polymer.

We now move from the effect of the polymer on mean flow properties to its influence on the velocity fluctuations about the mean. Figure 15 shows the rms fluctuations in the transverse velocity component as a function of X measured at $Y = 0$. The vertical axis is

$$v'(X)/U_f = \sqrt{\langle (v_y(X,t) - \langle v_y(X,t)\rangle)^2\rangle}/U_f,$$

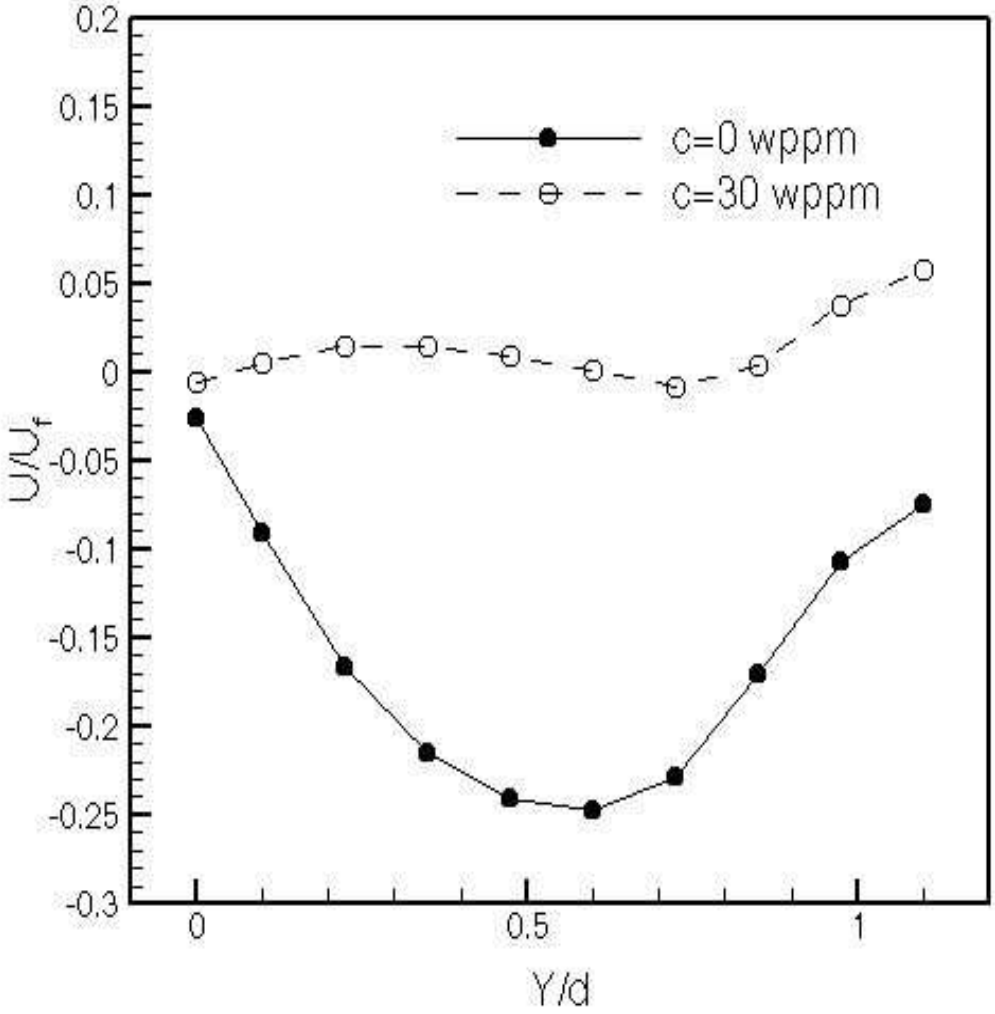

Figure 14: The normalized, time-averaged transverse velocity vs the transverse distance measured from the rod axis. These measurements were taken at point 2 mm downstream from the rod.

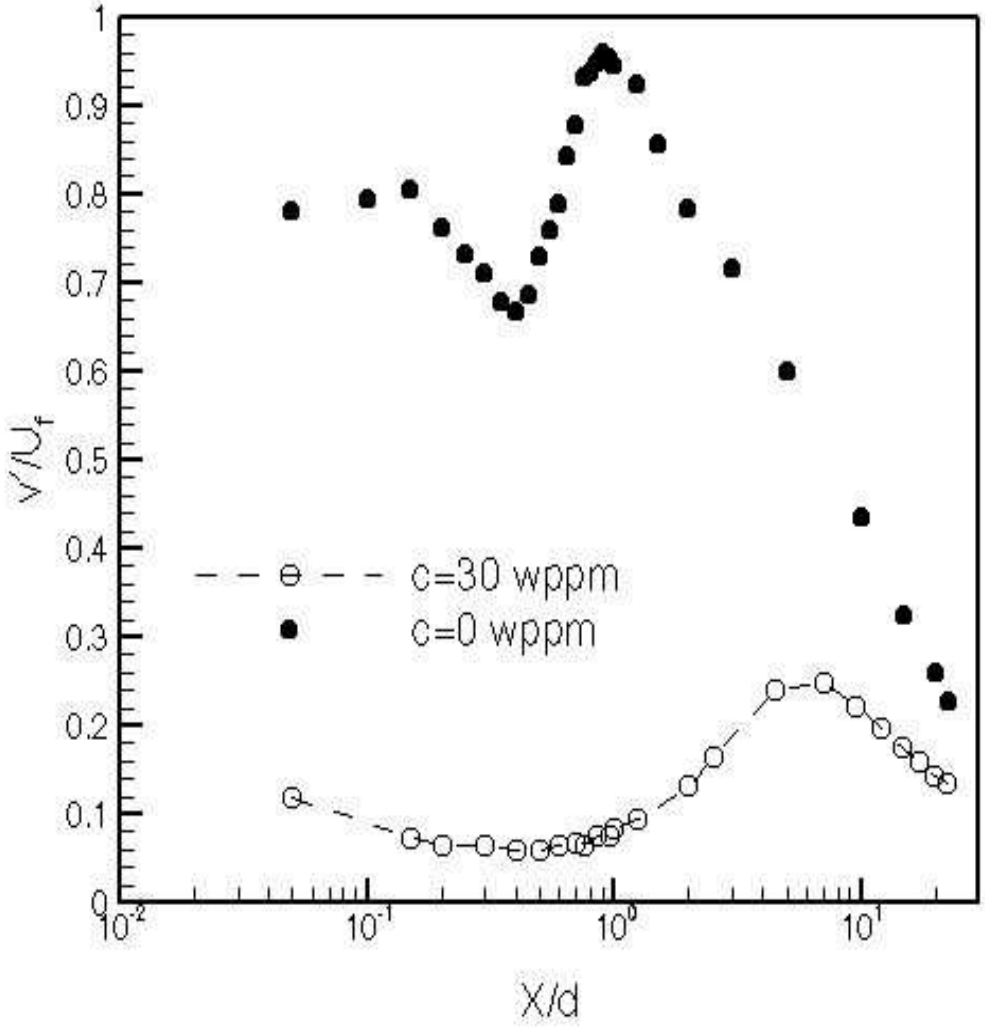

Figure 15: Transverse rms velocity fluctuations vs distance below the rod for the polymer-free (closed circles) and polymer-containing (open circles) films.

and the abscissa is $\log(X/d)$. Here $v_y(X,t)$ is the time- dependent transverse velocity component. Consider first the polymer-free measurements, designated as v_0' . The maximum value of the function appears at a position X called the formation length l_d . This length is comparable to that of the recirculation region present just below the onset of vortex shedding.[48] The open circles in Fig. 15 show the corresponding quantity v_{30}'/U_f with the polymer present. The formation length is increased six-fold and the maximum value of v' is dramatically reduced.

In spite of the increase in l_d produced by the polymer, it has little effect on the peak shedding frequency, as was previously observed,[37] but there is a measurable downward shift. The polymer's dramatic broadening of the frequency power spectrum $S(f)$ is seen in Fig. 16(a). These measurements were made at $X = 3$ cm and with $U_f = 200$ cm/s. The small downward shift of the peak frequency f_s is a robust result, but its magnitude does vary with concentration, albeit weakly. This downward shift was previously reported by Usui et al.[37, 49] In an attempt to understand the origin of the broadening of $S(f)$ for the polymer-containing solution, measurements were made of the spread in time intervals δt between successive zero crossings of $v_y(t)$. A histogram of the time intervals δt displays a broad distribution, which demonstrates that the time between shedding events is not constant. In addition, the amplitude of $v_y(t)$ also fluctuates, as was seen in a time trace of this variable. Whereas the spectral measurements were made using a PEO concentration of 30 wppm, spectra measured at concentrations as low as 14 wppm also showed a suppression of the peak in $S(f)$ and a broadening effect.

3.4 DISCUSSION

The measurements in Figs. 13 and 15 show that the polymer has a significant effect on the boundary layer, increasing the formation length several fold. This increase is consistent with the presence of an elongational viscosity term in the Navier-Stokes equation. The stretching of the vortex formation region by the polymer additive is accompanied by a suppression of the transverse velocity fluctuations, as seen in Fig. 15. Since these fluctuations are

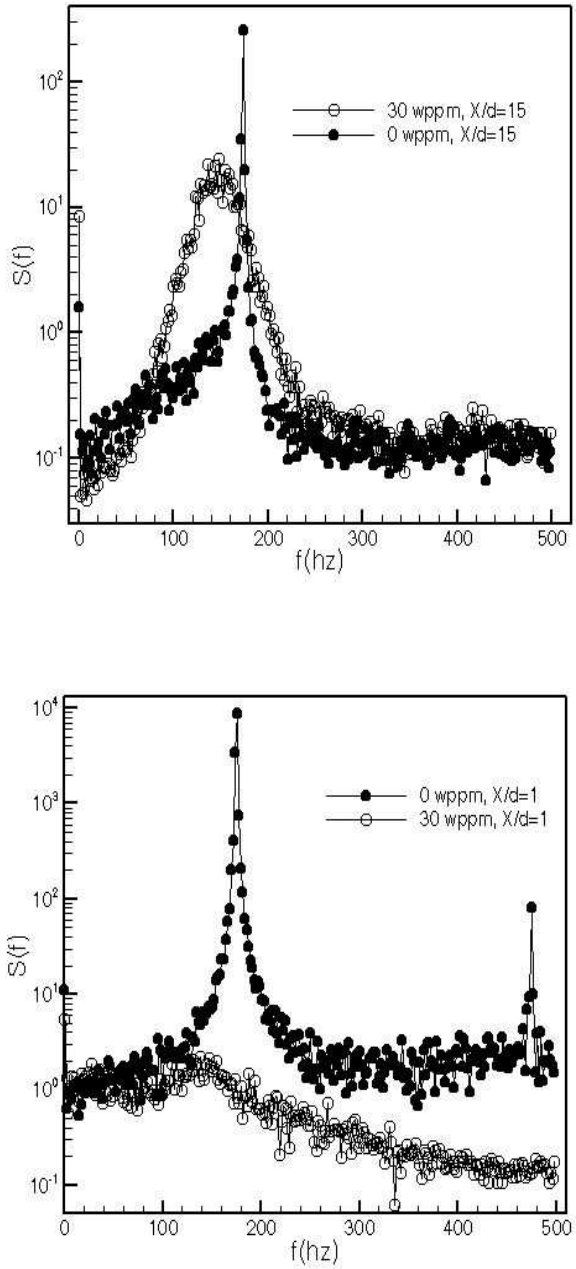

Figure 16: Power spectra for polymer-free and polymer-containing films. The spectra were measured at distances $X = 30$ mm below the rod (a) and at point very close to the rod, $X = 1$ mm (b). The peak in $S(f)$ is the shedding frequency, called f_s in the text.

instrumental in creating the vortex street,[35] it is perhaps not surprising that an array of staggered vortices does not immediately appear downstream from the rod, as in Fig. 12(a), but develops only at a larger value of X, as seen in Fig. 12(b).

It remains to be understood how the polymer strongly broadens the power spectrum $S(f)$ of the velocity fluctuations below the rod. The origin of this broadening could simply be the randomization of the passage of identical point-like vortices past the observation point, much like the randomness of a dripping faucet. On the other hand, its source might be the temporal variation of the velocity amplitude. Both of these effects are present in our measurements of $v_y(t)$.

The narrow width of $S(f)$ in the polymer-free soap solution (see Fig. 16(a)), closed circles establishes that the flow directly behind a rod is highly periodic. This periodicity is observed even within a diameter d of the rod, as seen in Fig. 16(b) (closed circles). The polymer additive strongly alters $S(f)$ near the rod, as is also seen in Fig. 16(b) (open circles). The height of the peak in $S(f)$ in Fig. 16(b) is four decades smaller than in the polymer-free measurements, demonstrating that the polymer suppresses the amplitude of the oscillations in $v_y(t)$ and broadens the spectrum as well. At X/d=1 there is hardly a remnant of a well-defined shedding frequency. It is clear from the spectra in Fig. 16 that the polymer additive does not destroy vortex shedding; it merely depresses it to a point further downstream. This observation is consistent with the measurements in Figs. 13 and 15, and the photographs in Fig. 12. Visual observation far below the rod reveals that the addition of the polymer does not significantly alter the ratio A of the lateral and longitudinal separation of the vortices. The measurements of A show it to be slightly lower than the Karman value of 0.28,[50] but the uncertainty in this ratio is large, namely $\pm$ .05.

3.5 SUMMARY

A small concentration of a polymer of high molecular weight is seen to strongly effect the creation and shedding of a Karman vortex street in a quasi-two-dimensional flowing soap film. The rms velocity fluctuations behind the rod are strongly suppressed by the polymer

additive. Our principal finding is that at a low concentration of $c = 30$ wppm, the rms fluctuations in the velocity are suppressed at all downstream points. This finding implies that the polymer strongly reduces the magnitude of the velocity fluctuations caused by the presence of the rod. The experiments further suggest that the origin of this effect is the introduction of an elongational viscosity term in the Navier-Stokes equation.

4.0 POWER FLUCTUATIONS IN A LIQUID CRYSTAL

4.1 INTRODUCTION

Recently, the nature of fluctuations of global quantities such as power dissipation in systems held far from equilibrium has become of intense interest [51, 52, 53, 54, 55, 56, 57]. Such spatio-temporal fluctuations in physical quantities are often as important as their mean values. This is especially true for systems that are far from equilibrium. Examples include violent storms, stock market swings, sun spots, volcanic activities and floods. In this work, the focus is on global fluctuations in a driven system that is held out of equilibrium by continuous injection of energy. This energy is ultimately dissipated as heat, and the mean system properties, e.g. its temperature, remain constant in time. It is useful to recall the case in equilibrium systems with macroscopic size, where the standard deviation σ_X of a global variable $\langle X \rangle$, such as energy or entropy, is such that $\sigma_X / \langle X \rangle \propto 1/\sqrt{N}$ where N represents the system size, because many statistically independent fluctuations are present. Even near a 2nd order phase transition the fluctuations will average out if the sample size is larger than the thermal correlation length. Moreover, there is the fluctuation dissipation theorem (FDT) which relates σ_X to the system's susceptibility to changes. For example the fluctuations in energy are related to the specific heat at constant volume[58].

For driven systems one cannot make such general statements about fluctuations in global quantities. The FDT does not apply, and there is no guarantee that $\sigma_X << \langle X \rangle$. However, when such a system is driven only slightly above its first bifurcation point, only a small number of spatially and temporally coherent modes will be excited. In this regime, we can study how the fluctuations are related to the small number of excited modes (or quasiparticles).

4.2 BACKGROUND

Boltzmann's ground breaking work in equilibrium statistical mechanics produced a method to interpret thermodynamics in terms of a molecular description. By appreciating the importance of entropy, or more accurately his H function, for equilibrium systems, he was able to show that their exist a most likely microscopic distribution for any give macroscopic state. The Boltzmann factor, which is Gaussian in momenta for an ideal gas, allows one to define the average of macroscopic quantities, such as pressure or energy. Ergodicity is the assumption that the temporal fluctuations of the individual positions and momenta of the elements of the system are sufficiently large to allow the sampling of all of available phase space. The definition of a statistical measure coupled with the assumption of ergodicity permits the equating of a time average to an ensemble average.

$$\langle f \rangle = \int_{\omega} \mu f d\omega \tag{4.1}$$

Here f is any macroscopic measurable quantity, μ is some measure or weight, and the integration is over phase space ω.

The same treatment has been sought for non-equilibrium systems. A statistical analysis of dynamic systems would appear to necessitate a dynamical measure. Unlike entropy, which is intuitively appealing, there is not an obvious quantity to maximize in non-equilibrium systems. It is this quantity, and the statistical distribution which maximizes it, that interests us.

The work of Gallavotti and Cohen (GC) hinges on the assumption that states with high entropy production are preferred over states with low (or even negative) entropy production. The most appealing aspect of this theory is that the dynamics are intimately involved in determining the ensemble average. The main prediction of the GC work is that the probability π of measuring an entropy production rate s_τ over a time τ follows the following relationship.: $\pi(s_\tau)/\pi(-s_\tau) = e^{s_\tau \tau}$. Here we have set $k_B = 1$. The author finds this theory a promising route towards understanding driven systems. For this reason the basics of the GC theory is outlined in Appendix E. It should be noted that the work of Crooks and Aumaitre [59, 56] are excellent alternative theories that address this issue. Perhaps it is simply serendipitious

that these theories produce the same relation as stated above. Simplicity suggests that this result may be universal.

It was the initial goal of this study to test the main prediction of this fluctuation theorem (FT). It proved to be impossible to measure any negative power fluctuations, and thus a direct test is not permitted. The experiment is outlined below, and any connections to the GC theory will be discussed.

4.3 LIQUID CRYSTALS

In an attempt to test the result of Gallavotti and Cohen we, measured the global fluctuations in power dissipation and light transmission through a liquid crystal just above the onset of electro-convection(EC). Liquid crystal are made up of rod like structures, whose anisotropic dielectric constant causes the molecules to align in the presence of and applied electric field. The spatial distribution of molecules produces regions of net charge at the boundaries of the sample, which will feel a net force from the applied field. If the field is sufficiently large the fluid will begin to convect.

It was not possible to confirm the main result of the GC theorem due to our inability to measure negative power fluctuations. It was however possible to establish a dynamical temperature and identify the modes responsible for fluctuations in injected power. The source of the fluctuations is found to be the creation and annihilation of defects. A defect is a local abrupt change in the alignment of the rod-like molecules. If the system is near equilibrium defects(black filaments and Schlieren structures) are present, and can be understood through a minimization of the systems free energy[60]. The defects studied here are due to a dynamical instability and hence cannot be described by an equilibrium theory. They are spatially uncorrelated and yet maintain some degree of temporal correlated. The temporal correlation is seen to persist for extremely long times.

In order to maximize the temporal fluctuations in any system, it is advantageous to minimize the number of modes, or quasi-particles in the system. For a liquid crystal this dynamical state exists just above the first bifurcation point. The principal bifurcation in EC occurs

above a critical driving voltage U_c, at the onset $\epsilon = (U/U_c)^2 - 1 \approx 0$ striped rolls appear in the plane of the liquid crystal (LC). As ϵ is increased slightly, defects in the roll pattern are formed and have a lifetime (see Fig. 17)[61] leading to a state often called defect turbulence [62, 63]. We have found that defects are spatially uncorrelated. Nevertheless, temporal correlations in P are persistent, indicating an underlying order to this chaotic system and permitting the definition of a sharply defined frequency f^* .

The experiments were performed on planarly oriented (nematic director parallel to the bounding glass plates) LC samples of methoxy benzylidene-butyl aniline (MBBA)(University of Pittsburgh and Kent st.), Phase V (P5) [64] and Mischung 5 (M5)(Kent St.) [65]. All samples have been prepared with appropriate electrical conductivities and the measurements were made under temperature-controlled conditions. The active area A of the samples was varied between A $\sim$ 0.01 cm^2 and 1 cm^2 while their thickness d ranged between (16.6 $\pm$ 0.2)μm and (52 $\pm$ 1)μm, providing aspect ratios s $=\sqrt{A}/d$ from 36 to 602.

4.4 EXPERIMENT

4.4.1 Cell construction

Sample cells are constructed from two glass plates coated with indium-tin oxide (IO). The plates are a few mm in thickness, and are typically cut into 3 cm by 5 cm rectangles. The plates are epoxied together, separated by thin plastic spacers which ranged from 25 to 125 μm, and filled with liquid crystal. The actual area of the sample is determined by etching away most of the IO from both plates leaving only a thin strip of conducting material running down the center of the plates. The intersection of these two strips defines the active sample area.

Etching is performed by masking off the desired area with clear tape, and swabbing the entire sample with diluted hydrochloric acid. In order to activate the reaction, zinc powder is sprinkled onto the plate. After about a minute the acid and zinc powder are rinsed off, and the tape is removed. By performing the process twice, i.e etching halfway from one edge, and then slightly less then half from the opposite edge, it is easy to produce thin, mm-wide,

stripes.

Once the plates are properly arranged with the plastic spacers in place, the sample is epoxied together at two of the overlapping edges. This method permits the addition of the liquid crystal after the plates have been fixed. Typically capillary force is sufficient to pull the liquid crystal into the reservoir between the plates. If bubbles form, their removal is possible by placing the sample in a partial vacuum for several minutes. The liquid crystal used in the experiments at the University of Pittsburgh was methoxy benzylidene-butyl aniline (MBBA). The two open edges of the sample are then sealed with epoxy, and wires are attached to the IO electrodes with silver epoxy.

4.4.2 Global power and transmitted light measurements

In order to stabilize the mean power dissipated by the liquid crystal, the sample is placed in a copper block which is then emersed in a tank of water. The water temperature is kept constant by a heater with a tronac feed back loop. This scheme limits temperature fluctuations to within 10 mK, enabling measurement times of at least several hours.

An ac voltage generated by a signal generator was stepped up (2 or 4X) with a transformer and then applied across the sample. The behavior of liquid crystals is frequency dependent with a transition at f_c of roughly 500 Hz. The frequency was fixed at 100 Hz in the experiments reported here.

An ac voltage was measured across a resistor(50 or 100 kΩ) placed in parallel with the liquid crystal. The signal was filtered and boosted by a preamplifier before going into a lock-in amplifier(LI). The LI was tuned to the driving frequency in order to remove all fluctuations due to the drive. This method was essential to measure the relatively small temporal power fluctuations. The output of the LI is then sent into another amplifier before being sent into an analog to digital converter in a PC. The indicated time traces of power fluctuations in Figure 18 establish that the relevant fluctuations are much slower then the driving frequency. An analog to digital board was then used to capture the signal at a rate of 16 Hz. Histograms of the power fluctuations, autocorrelation functions, and other measurements were performed with in-house software.

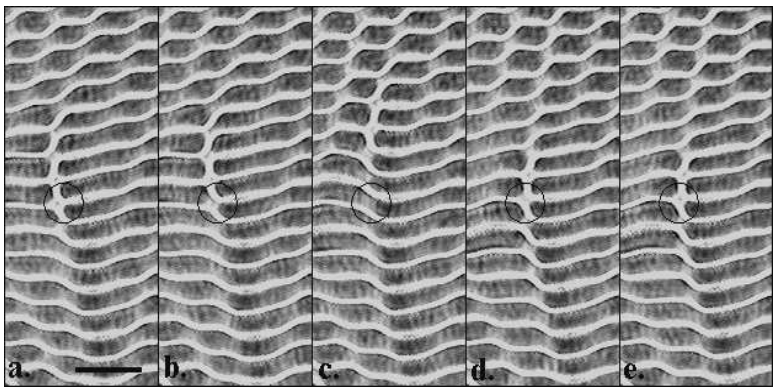

Figure 17: The evolution of a defect can be seen in the circle. The frames were taken at t = 0, 1, 15, 26, 27 sec. The M5 sample has an aspect ratio s=136, and $\epsilon \simeq 0.2$.

Video images of the convecting liquid crystal were taken using an inverted microscope. The sample was illuminated from the back, and the roll patterns were apparent without the use of cross-polarizers. Video images were recorded using a frame grabber board, and a PC interface. Spatial and temporal correlations were performed using in-house software.

4.4.3 Quasi-particles, power fluctuations and persistent oscillations

In order to identify the modes responsible for fluctuations in power injection, we record the time dependent power, P(t), optical patterns, and the transmitted light intensity I(t) integrated over the entire area of the sample.

Fig. 18 shows time traces of both P(t) and the integrated transmitted intensity I(t) at $\epsilon = 3.0$ and at $\epsilon = 0.78$. The means have been removed, and the and decays signals have been made dimensionless, by dividing by there respective standard deviations. Observe that both of these global measures exhibit a dominant frequency f* that increases with ϵ. The relative phase between the signals is arbitrary. Note that low frequency quasi-periodic oscillations in I(t) were also detected in Refs. [66] both in local and in global measurements.

The characteristic frequency f^*, is also seen in the normalized autocorrelation function $g_a(t) = \langle P(t')P(t'+t)\rangle / \langle P(t')\rangle^2 - 1$. At $\epsilon \simeq 0.124$, where EC rolls are well developed but there is no defect creation/annihilation, $g_a(t)$ does not oscillate but decays within 60 seconds.

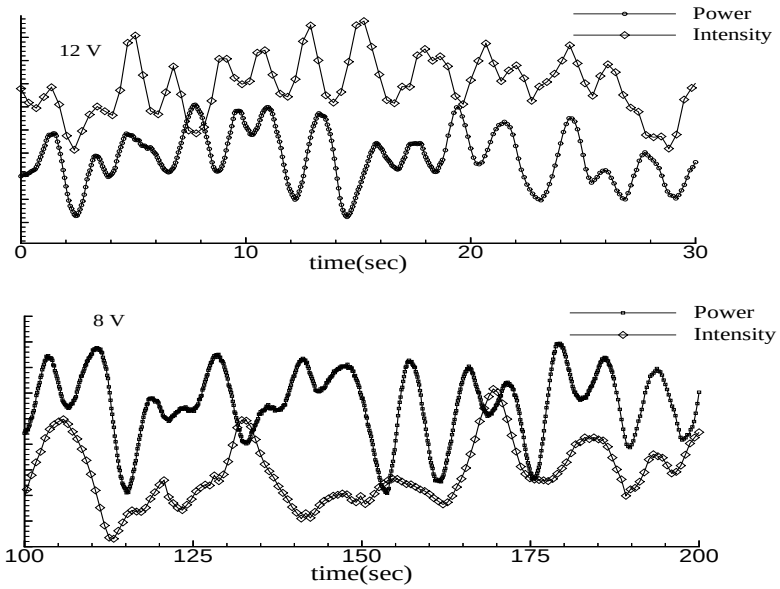

Figure 18: Time traces of power, and transmitted light intensity at ϵ values of 3.0(upper curve) and 0.78(lower curve)

When the 'varicose' [67] pattern develops in M5 at ϵ= 0.2, the motion of the rolls starts with infrequent generation/annihilation of defects, $g_a(t)$ exhibits slow oscillations at frequency f^* . With further increase of ϵ, f increases until $\epsilon \simeq 5$. Above $\epsilon \simeq 5$ the oscillations vanish as their amplitude disappears into the noise. At this point, optical observations reveal the liquid crystal is fully in the dynamic scattering mode 1 [68], where the rapid creation/annihilation of dislocations takes place.

In the range of ϵ for which oscillations in $g_a(t)$ are seen, they appear to be truly persistent. That is, even for measurement times of many hours, the oscillations persist for the length of the run (10^4 oscillation periods). These measurements were at a value of ϵ where the sample contained many hundreds of defects. It is truly striking that such a large number of spatially uncorrelated defects gives rise to oscillations in $g_a(t)$ which persist for the entire length of the measurement. Figure 17 displays a series of photographs made at the indicated times t. The liquid crystal is M5 having a thickness, d = 52 μm. In this relatively thick sample, the 'varicose' pattern persists down to ϵ = 0.2. At this low level of excitation, the number of dislocations is relatively small and the roll motion is slow. At t = 0 we begin watching

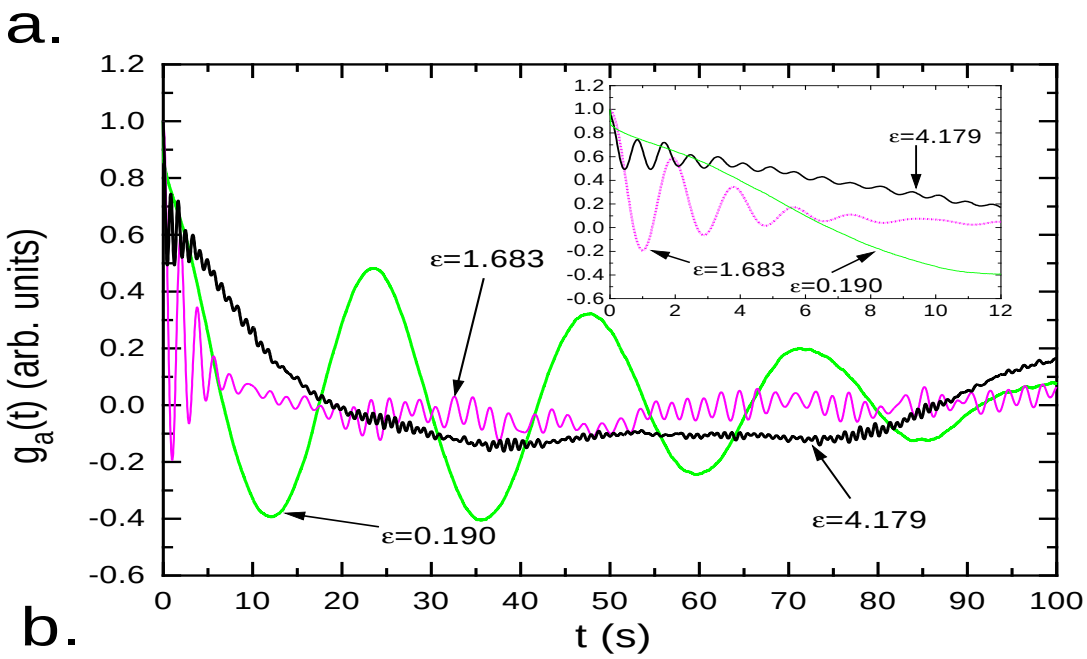

Figure 19: Autocorrelation function of temporal power fluctuations for the designated values of ϵ

a single defect of interest (marked with a black circle) as it starts to annihilate Fig. 17(a). One second later the annihilation process is finished Fig. 17(b) and a defect is created at the same location about 26 s later (Fig. 17(d)-(e)). Note, there is a slight difference in the position of the defects in Fig. 17(a) and (e) due to the slow climb motion [69]. The lifetime of a defect measured in this manner is within 5 percent of the inverse of f* determined from $g_a(t)$ for power fluctuations.

Optically tracking dislocations is problematic because their number increases and their lifetime decreases with increasing ϵ. The frame grabber has limited time resolution, and when the dislocations are too close together it becomes difficult to track then. Measuring power fluctuations has no such limitation.

The spatially integrated transmitted light through the liquid crystal also reveals periodic oscillations. Figure 20 is a plot of the average period for oscillations measured from power fluctuations(closed diamonds), as well as the total integrated light intensity(open circles). These values were obtained from the temporal separation of subsequent peeks in the autocorrelation function for either variable. These two quantities were measured in the same sample, but not simultaneously. The existence of the same oscillation periods shows that the two quantities are most likely driven by the same mechanism. Although it is difficult to identify single defects, a study of the evolution of visual global structures may be an extremely powerful tool in this study.

We submit that this close agreement leaves little doubt that dislocations are the localized excitations responsible for fluctuations in the global, dissipated power. Thus, having identified the source of the fluctuations as the defect lifetimes, we are able to determine the average lifetime of a defect beyond the range where it is possible to do so optically.

4.4.4 Probability of fluctuations

Figure 21 is a histogram of the power fluctuations, $P - \langle P \rangle$, normalized by the standard deviation $\sigma_P = \sqrt{\langle (P - \langle P \rangle)^2 \rangle}$. Here the abscissa is plotted in terms of $((P - \langle P \rangle)/\sigma_P)^2$. Plotted in this way it is clear that the distribution is Gaussian out to 3 standard deviations. This behavior does not contradict the predictions of the GC theorem, however it could also

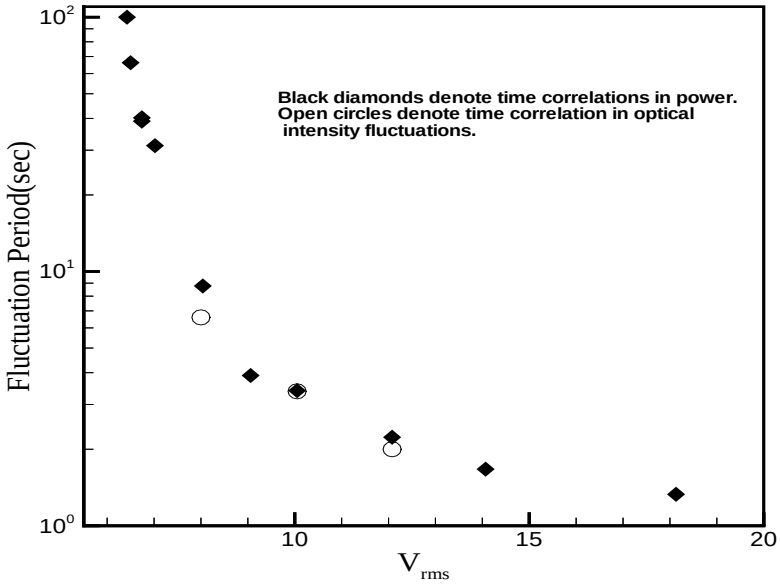

Figure 20: The average lifetime vs the driving voltage. The measurements were extracted form global power measurements (black diamonds) and global intensity measurements (open circles) in MBBA.

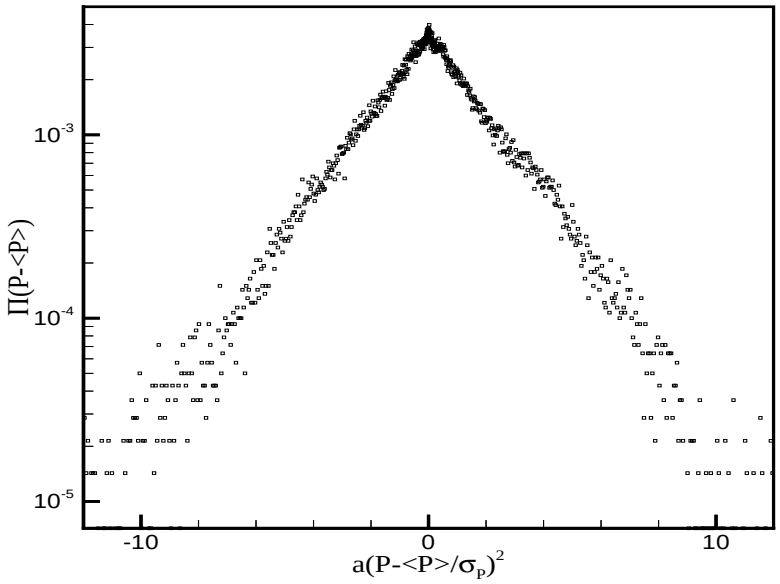

Figure 21: Histogram of power fluctuations

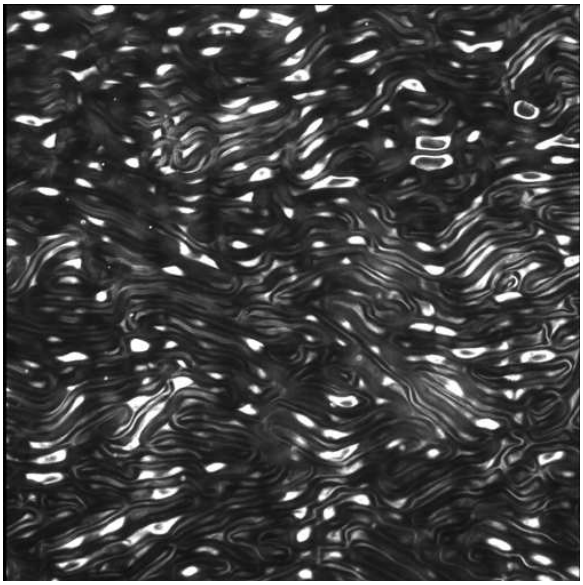

Figure 22: Image of Turbulent Liquid Crystal $\epsilon = 3$. The width of the image is approximately 100 μm

be easily understood in terms of the central limit theorem. Several hundred thousand points were used to produce this distribution, spanning several hours, and thousands of oscillations. The central limit theorem is based on the idea that many uncorrelated measurements have taken place and added up. As we have already seen the system displays temporal correlations, yet it appears to be composed of spatially random elements. One should not infer from the persistent oscillations in the temporal correlation function any degree of long time causality.

At small ϵ the evolution of a defect can be easily tracked as in Fig.17(a-e). However as the LC becomes turbulent it is difficult to identify an individual defect which is apparent from Fig. 22. Here the system is composed of many, on the order of hundreds of worm like rolls. These structures are continuously moving and interacting. Measurements of a spatial intensity correlation function, $\mathcal{I}(\nabla) = \langle(\tilde{I}(x)\tilde{I}(x+r))^2\rangle/\langle\tilde{I}^2\rangle$, does not provide any significant correlation length. Here $\tilde{I}$ is the intensity with the mean subtracted out. These measurements, not shown here, confirm that the system is not spatially coherent. Visual observations show that the behavior of nearby rolls is correlated, but only over an order of a few rolls. It is this spatial incoherence that gives credence to the applicability of the central

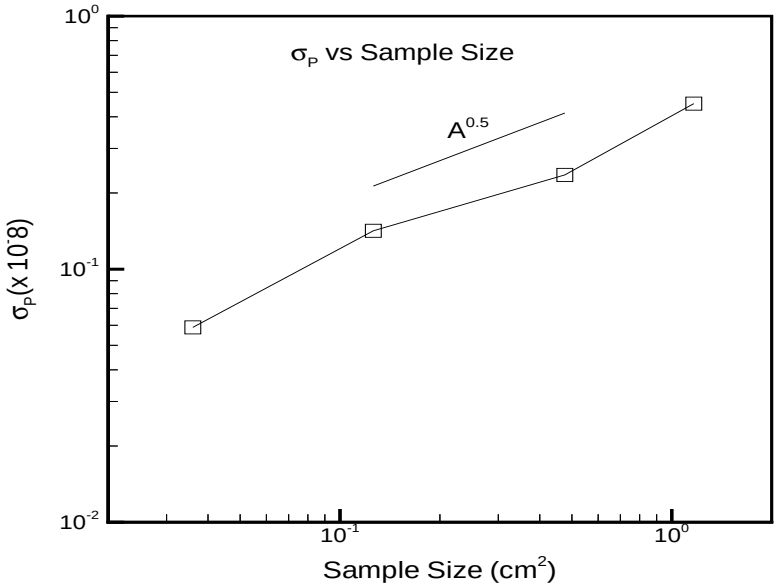

Figure 23: Standard deviation versus sample size. $\epsilon = 1.78$

limit theorem.

Further evidence for spatial incoherence is exhibited in figure 23. Here the standard deviation is plotted versus the area of the system. For large values of ϵ the average length of a continuous roll becomes comparable to the width of a roll, therefore making the number of defects proportional to the system size. The line in the graph has a slope of 0.5 indicating the fluctuations increase as the square root of the sample size or equivalently the number of defects, N. The relationship $\sigma_P \propto \sqrt{N}$ is indicative of a system of random sources.

Figure 24 shows the dependence of the normalized variance in power fluctuations, $\sigma_P/\langle P\rangle$ versus the control parameter. As ϵ is increased past a value of 0.2, $\sigma_P/\langle P\rangle$ quickly climbs. Simultaneous optical observations reveal the spontaneous creation and annihilation of defects begins near the same value of ϵ, where the stationary EC rolls break up into moving segments. The number of rolls, and the rate of defect number variation increases rapidly along with the normalized power fluctuations up to a value ϵ close to 1.7.

As the control parameter is increased even further, $\sigma_P/\langle P\rangle$ falls off. Data not presented here shows that $\langle P\rangle$ increases linearly with the driving voltage, as would be expected for a purely resistive system. The non-monotonic behavior is therefore due to a levelling off of the

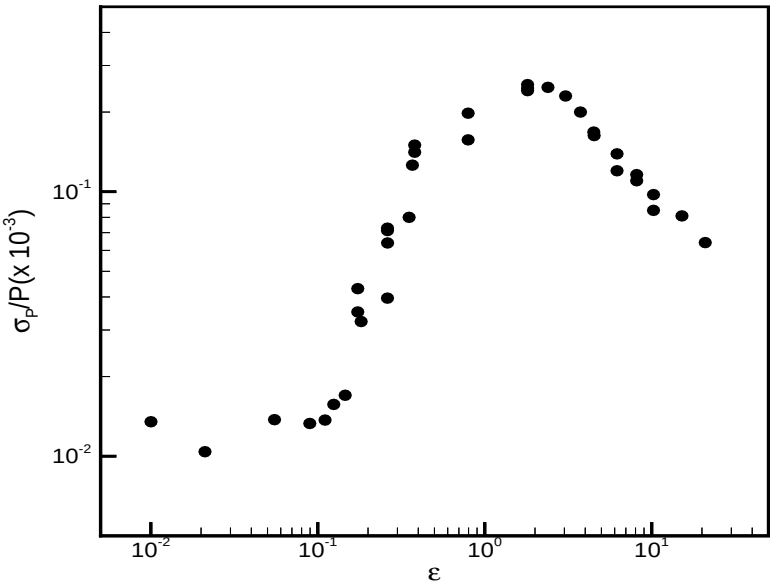

Figure 24: normalized power fluctuations plotted against the control parameter ϵ

fluctuations in injected power.

4.4.5 Dynamical temperature, The Fluctuation Theorem and liquid crystals

In an attempt to connect experimental observations with the FT, we relate the entropy production rates, s_τ, over a time τ, with the power injection through the thermodynamic relation $P = s_\tau k_B T_{ss}$. Here k_B is Boltzmann's constant, and T_{ss} is a dynamical temperature[70]. The dynamical temperature is the steady-state equivalent to the thermodynamic temperature for systems far from equilibrium. Whereas the thermodynamic temperature is related to the kinetic energy of the molecules of the system, T_{ss} is a function of the kinetic energy of the relevant modes, or quasi-particles in the driven system, i.e. $k_B T_{ss} = 1/2Mv^2$ plus energy required to make or destroy a defect. The energy needed to create a defect is estimated from the elastic coefficient K for MBBA[60], which is 10^{-12}N/m and the typical size of a defect which can be taken to be the separation of the plates (typically $50\mu m$).

The main result of the FT relating the ratio of probabilities for positive and negative entropy production rates, does not make any prediction for the form of $\pi(s_\tau)$ itself. It is easy to

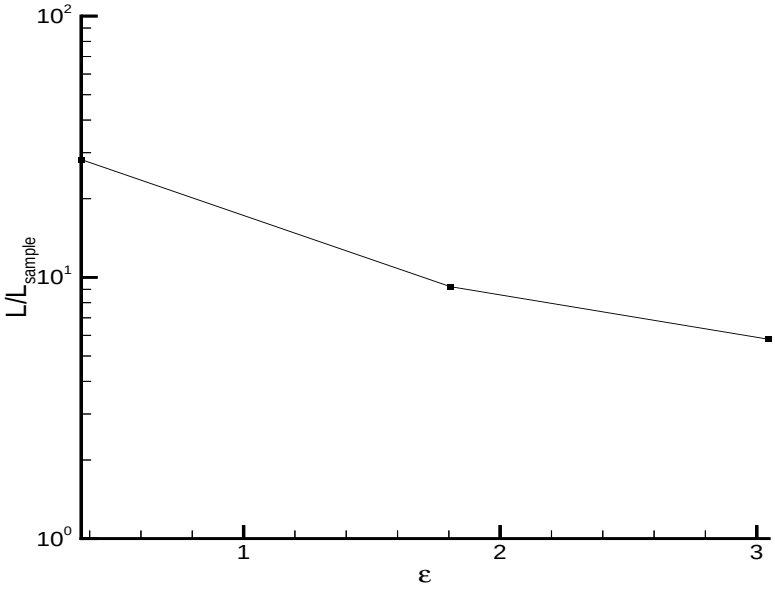

Figure 25: The normalized mode size plotted versus the control parameter ϵ.

show that a Gaussian distribution, $\pi_\tau(P) \propto exp[-(P - \langle P \rangle)^2/(2\sigma_p^2)]$ is consistent with the theoretical result, which is found in the experiments[70]. It can then be shown:

$$\sigma_P/\langle P \rangle = \sqrt{2k_B T_{ss}/\langle P \rangle \tau} \tag{4.2}$$

The velocity of a roll can be approximated by $v_{rms} = v_0\epsilon$ were v_0 was found to be 16μm/s. The size of a mode can then be determined using the density, ρ, for MBBA and the thickness of the sample. Figure 25 is a plot of the calculated size of a mode normalized by the sample length, and plotted against the control parameter ϵ. It is apparent from this figure that the predicted length is nearly an order of magnitude larger then the sample size for even the smallest ratio. Here the creation/annihilation energy was not used to determine the predicted length, however if this energy is approximated by the elastic coefficient K times the size of a mode the result is only changed slightly. This finding makes it difficult to relate the GC predictions to our findings. A discussion of this point is presented below.

4.5 CONCLUSION

4.5.1 Gallavatti and Cohen

The lc measurement raise doubts about the applicability of the theory to these measurements. The predicted mass of quasi-particles is at least an order of magnitude larger than the sample size. This observation implies that the observed dynamic fluctuations are not large enough to produce the relatively large deviation in power fluctuations. In addition the FT predicts a monotonic increase in $\sigma_P/\langle P\rangle$ as a function of ϵ, where we clearly see a maximum around 1.7. There are several possible reasons why the GC theorem is not confirmed.

Most importantly, we measure the fluctuations in the power injected into the liquid crystal, not the power dissipated, which is at the core of the theory. Intuitively one may expect these two quantities to fluctuate with the same magnitude. It is however conceivable that the deviation in the dissipated power is much smaller.

The boundaries in this system remove a significant amount of energy from the liquid crystal. The action of the plates is inherently irreversible, being incapable of storing and reinjecting energy into the fluid. Although these inconsistencies undermine the relevance of this theory, they do not account for the surprisingly large value of the fluctuations.

The discrepancy between theory and experiment could also be accounted for in view of an amplification effect. If one imagines the LC to be a network of passive and active circuit elements, (resistors, capacitors, and inductors) whose connections are continuously altered by dynamical fluctuations, it is possible that large impedance, and hence large power fluctuations could be caused by moderate dynamically induced structural changes. In other words a relatively small change in the kinetic energy in the liquid crystal due to defect evolution could produce a large fluctuation in the power injected into the sample. The results of this experiment in know way disprove the Fluctuation Theorem. We only assert that given our assumptions for typical velocities, and distortion energy the size of the relevant modes would need to be much larger than the sample size.

4.5.2 Temporal coherence and random statistics

The most surprising and interesting outcome of this study are the persistent temporal fluctuations in the autocorrelation functions for both power and transmitted intensity. In order to explain the existence of these oscillations in the face of disorder one is forced to acknowledge some global mechanism. At the same time several measurements including $\pi(P)$, σ_P vs. N and spatial correlations depict a system composed of elements of random strength.

The most tangible is that the system is experiencing a global mean flow. Recent work done in Rayleigh Benard convection[71] predicts the persistent slow frequency oscillations in the velocity of a flow driven by temperature induced buoyancy fluctuations. In the Rayleigh Benard system the interaction of hot and cold plumes leads to a stable global flow. Although the mechanism for this large scale flow in an LC has not been identified, such correlated motion could be responsible for our observations. However such large scale motion is not apparent visually and may only be detectible through a detailed analysis of the evolution of the roll pattern.

It is also possible that the temporal coherence is due to a competition between energy, and entropy. Visual observations indicate that local roll structure does appear to be correlated to the intensity fluctuations. In the analyzed pictures, rolls appear dark, and regions between the rolls light as seen in Fig. 22. Images with relatively low light transmission have several large regions with very straight rolls, whereas when the intensity is high the flow consists of more buckled rolls. This correlation between high intensity and buckled rolls makes sense since a curved roll produces larger regions of open (roll free) areas.

A sample filled with straight rolls occupies a smaller volume in configuration space than one with many curved rolls. In this manner I propose that a dark image indicate a lower entropic state then a light image. Because the boundary conditions counteract the bending of rolls, the stress is released by straightening the rolls and topological defects are left behind. It would appear then that a state with many straight rolls (dark) would be in a relatively low energy state. Preliminary measurements show oscillations in the rather short correlation length, however much more work is needed to make a definitive connection between power dissipation and global roll structure.

A clear understanding of the temporal fluctuations is still being sought. Hopefully better imaging techniques will allow the measurement of any mean flow. Measuring P while simultaneously capturing images of the sample will help establish the structure of the flow during instances of high and low power injection.

APPENDIX A

TURBULENCE

A.0.3 Scales

A turbulent flow can be characterized by several length and time scales. Three relevant length scales for three dimensional turbulence are the outer scale of the turbulence l_0, the dissipation scale η, and the Taylor microscale, λ. The outer scale is defined as the integral of the normalized velocity autocorrelation function $C(R) = \langle \mathbf{v}(\mathbf{x}+\mathbf{R}) \cdot \mathbf{v}(\mathbf{x}) \rangle / \mathbf{v_{rms}^2}$. Beyond some finite distance the product of velocities separated by a distance R become random, and the the above average goes to zero. The integral is performed over the separation R and should be taken to infinite separations. However, experimentally we are limited to the largest image size, which is approximately 20 cm. The measured value of the outer scale is approximately equal to the theoretical value once the integral is performed over distances where the correlation function, $C(R)$, fluctuates about zero, providing a net zero contribution to the integral. The brackets indicate an average over points x,y and over many images. Here $v_{rms}^2 = \langle [v_i(x,y) - \langle v_i(x,y) \rangle]^2 \rangle$ where i is one of the two arbitrarily chosen directions in the horizontal plane. This quantity gives an estimate to the largest correlated structures in the flow. In other words, the relative motion of fluid elements separated by distances larger than the outer scale will be random. Separate experiments, not presented here, established that the turbulence is almost isotropic in the horizontal plane. For the surface, the value of l_0 is approximately 3.6 cm and for the bulk it is roughly 3.1 cm a few mm's below the surface.

In the Kolmolgorov paradigm energy is transferred essentially loss-free through intermediate

scales, or the inertial range. It has been shown that the inertial range spans all the way down to the Kolmolgorov dissispation scale $\eta(\nu^3/\epsilon)^{1/4}$ [6]. Where ν is the kinematic viscosity and ϵ is the energy injection/dissipation rate. The quantity ϵ is found using the following relation. $\epsilon = 15\tilde{\eta}\langle(dv_x/dx)^2\rangle$, where $\tilde{\eta}$ is the viscosity of water(1 cp). Experimental limitations did not permit spatial resolution of the velocity fields below 1 mm. Therefore the velocity gradients used to determine ϵ are only approximate. Since gradients only increase with decreasing scale,(above η) this gives a lower bound for ϵ, and hence an upper bound for η. For measurements in both the bulk, and the surface, η was found to be no larger than 0.1 mm.

The Taylor microscale is defined as $\lambda = \sqrt{(v_{rms}^2)/\langle[dv_x/dx]^2\rangle}$. The Taylor microscale Reynolds number is $Re_\lambda = v_{rms}\lambda/\nu$. The Taylor microscale is larger than η, and can be thought of as the size of the smallest energetic eddies in the flow. For the surface flows, λ is typically a few millimeters.

The turbulence is also quantified by three time scales. The first two are based on the above-mentioned spatial scales namely, the Kolmogorov dissipation time τ_η and the largest eddy turnover time τ_{l_0}. Both times are determined by $\tau^{-1} \equiv \Delta v/\Delta x$, where Δv and Δx are determined at the dissipation scale and the integral scale for τ_η and τ_{l_0} respectively. Once again experimental resolution only allows a limiting value for τ_η, which is found to be no longer than 1/80 sec. The largest eddy turnover time is found to be on the order of 1 sec.

The third relevant time scale is the lagrangian correlation time $\tau_{\mathcal{L}}$, defined as $\tau_{\mathcal{L}} = \int\langle\mathbf{V}(0)\cdot\mathbf{V}(s)\rangle ds/\langle\mathbf{V}^2\rangle$. Here $\mathbf{V}$ is the velocity of a lagrangian tracer, as measured in the laboratory frame. This time gives a quantitative measure of the temporal correlation of the lagrangian flow field. Preliminary measurements of $\tau_{\mathcal{L}}$ show that it is finite, and no longer than a few seconds.

The Navier-Stokes equation can be parameterized by the Reynold's Number, $Re = VL/\nu$. Typically these values are determined by the outer scale, l_0 (or integral scale), and the rms velocity. This Reynold's Number can be interpreted as a comparison of the size of the largest structures in flow to the smallest relevant scale.

The Reynolds Number used here is based on the rms velocity, and the Taylor microscale. Therefore the quoted Reynolds numbers are only an upper bound. The Reynolds numbers

determined by the outer scale and the Taylor microscale are related by, $Re_\lambda \simeq Re_{l_0}^{1/2}$. The value of Re_λ, which typically lies between 100 and 200, is presented for all of the measurements.

APPENDIX B

PARTICLE TRACKING AND ANALYSIS

All of the measurements performed in the surface experiment utilized particle tracking. There one illuminates seed particles with a horizontal sheet of laser light and tracks their motion photographically (see Fig. 3). Pairs of images are then used to track the motion of an entire field of particles from one instant to the next.

Image acquisition was accomplished in one of two ways. A commercial PIV (particle imaging velocimetry) system was used to capture images separated by very short (μsec) intervals. The PIV system is composed of a pulsed neodymium-doped yttrium aluminum garnet (Nd-YAG) laser, a charge-coupled-device (CCD) camera, a synchronizer board, and a frame grabber board. The laser is sent through a cylindrical lens in order to produce a sheet of light approximately 10 cm wide and 5 mm thick. The synchronizer board provides triggers for the camera, laser, and frame grabber board to allow the capture of very rapid, subsequent images. The frame grabber is installed in a workstation, and the images are stored directly to the computers memory. This device is only capable of capturing pairs of images at a maximum rate of 15 Hz, which does not allow for extended temporal measurement needed for lagrangian studies. Therefore, this apparatus was only used for the measurements of spatial structure, and single point measurements. The commercial PIV algorithm was not used to track particles, rather in-house software was used to perform this task.

The second method involves the use of a high speed video camera. Here the illumination is provided by a diode-pumped laser. The laser produces continuous light, and has a maximum output of 5.5 W. The camera has onboard memory, and can capture data at a rate of 1,000

frames per second at the highest resolution (1024 by 1024 pixels) for up to two seconds. The measurements presented here were generally taken at a rate of 400 Hz enabling one to track particles for several seconds. The images are then downloaded to a workstation, where in house software is used to determine the trajectories of the illuminated particles.

The floaters were particles of various diameters ranging from 10 to 200 μm. Most of the particles used were nearly neutrally buoyant. These include hollow glass spheres, polystyrene spheres, lycopodium spores, and talcum powder. Whereas lycopodium is hydrophobic, most of the neutrally buoyant spheres are held on the surface by surface tension. All of these particles must be spread uniformly on the surface of the tank at the beginning of a run.

Most recently highly buoyant spheres, having a specific gravity of 0.25, were used. These spheres can be added to the surface from the bulk. The flow can be seeded continuously, and uniformly over the surface throughout the length of a run. The interior measurements were made using neutrally buoyant polystyrene spheres of diameter 10 μm.

The correlation algorithm used to match particles from image to image was developed my Michael Rivera. This algorithm was unaltered for implementation in these experiments.

High particle density in combination with high compressibility causes particles to become very close together. These effects will frustrate even the best algorithms, resulting in the loss of particles. High shear is also responsible for errors in tracking. In general, seventy five to eighty percent of the particles identified by the tracking program are tracked. This percentage is rather good considering a typical field contains nearly 30,000 identified particles. The algorithm produces very adequate velocity fields. The spatial resolution is limited primarily by the density of particles in a field, and ultimately by their size.

Tracking an individual particle for several frames becomes quite difficult. Even very small fluctuations in the surface height can produce time varying illumination of particles, making it difficult to identify an individual particle over a sequence of images.

For these reasons we abandoned the idea of tracking real imaged particles. Instead we used the highly reliable velocity fields to advect an initially uniform distribution of simulated particles. The method of mapping these particles over a time step is quite simple. The velocity at every point is determined by an average of the local vector field. Figure 7 shows an evolved field of simulated tracers. The structures in the particle field are qualitatively

similar to those in Fig. 1, showing that this method is an effective means of capturing the behavior of this system.

APPENDIX C

SURFACE CONTAMINATION

Contamination is always a problem in any physical experiment. The effects of contaminants on flow is interesting and very important to practical real-world applications. Soapy molecules, or amphiphiles can form a monolayer film on an exposed surface of water [72]. These molecules can be introduced into the water through the air, any plastic surfaces, or contact with ones skin. Therefore filtering, or replacing the water was not sufficient to remove this surface "skin".

The monolayer greatly affects the flow, making the rms velocity fluctuations of the surface particles significantly less than that of the neutrally buoyant particles moving a few mm's or so below the surface. To further illuminate the effects of the surface contamination, we present measurements of the second order structure function on a dirty surface in contrast to a clean surface as shown in fig. 4. Figure 26 is a log-log plot of $D_2(r)$ on a contaminated surface. Here the oscillating grid was used, and positioned at $Z = 18.2$ cm (closed circles) and for $Z = 8.2$ cm (open circles), below the surface. The grid oscillation frequency for the two sets of measurements are indicated. The outer scale of the turbulence l_0 at Z=18.2 and 8.2 cm are 1.5 and 3.6 cm, respectively. The Taylor microscale Reynolds numbers Re_λ are 80 (Z=8.2 cm) and 50 (Z=18.2 cm). The measurements in Fig. 26 suggest that $D_2(r)$ is approaching its saturation value $2v_{rms}^2$ at large r. At smaller scales r, one finds that $D_2(r) = r^\chi$, with χ =1.6 and 1.4 at $Z = 8.2$ and 18.2 cm, respectively. The dissipative range at even smaller r, where $D_2(r) = r^2$, was not accessible. [6]. Here we see that the surface contamination greatly alters the form of $D_2(r)$. In fact the exponent χ is closer to what one

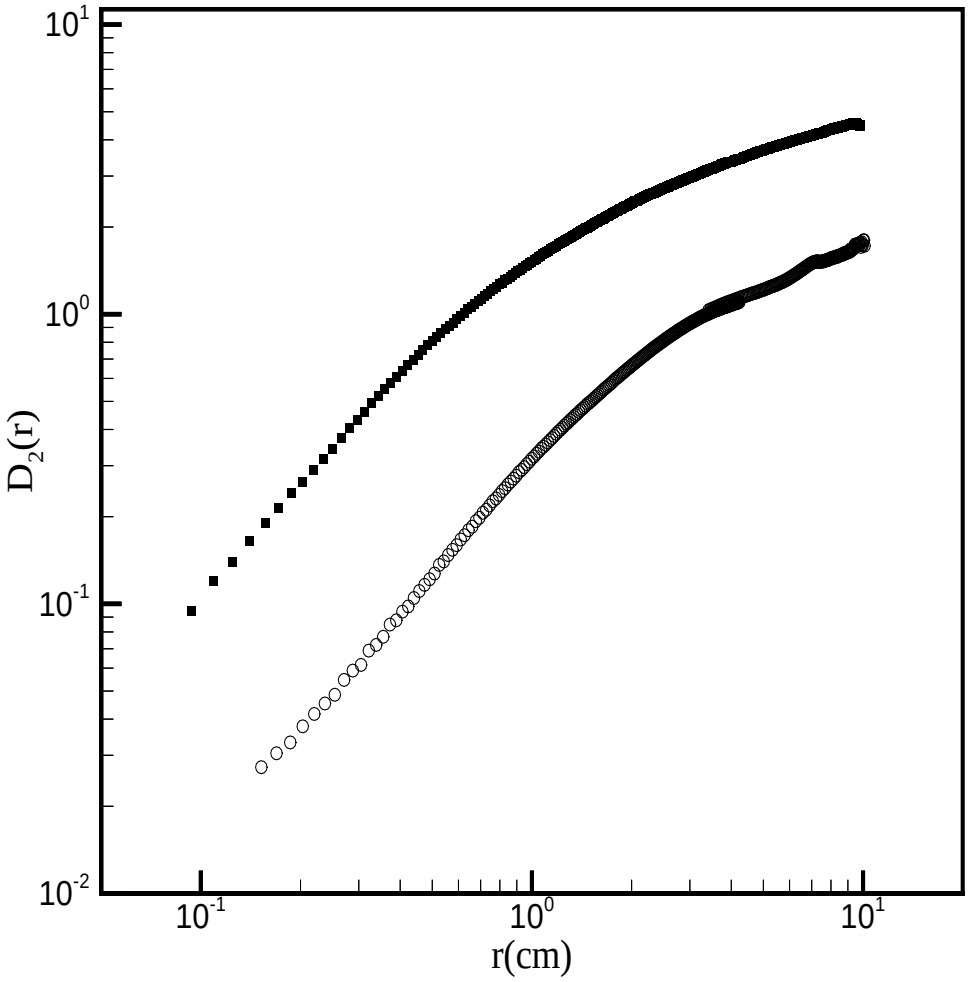

Figure 26: Log-log plot of the second moment of the (longitudinal) velocity difference at the indicated distances (Z) between the surface and the oscillating grid. The oscillating frequency of the grid and the surface-to-grid distances, Z, are indicated. Other parameters are Z=8.2 cm: $Re_\lambda = 80$, $l_0 = 3.6$ cm,$v_{rms} = 1.27$ cm/s; Z = 18.2 cm: $Re_\lambda = 50$, $l_0 = 1.5$ cm,v_{rms}= 0.7 cm/s. For both sets of measurements, $\mathcal{C}$=0.5± 0.1.

might expect for the viscous scale.

This amphiphile monolayer is also capable of producing extremely long-distance correlations. It is this long range interaction that gives way to a practical, and highly efficient method of continuously cleaning the surface.

The particles used for measurements will eventually effect the flow if their density becomes too high. The skimmer shown in Fig. 27 was developed to remove contaminants and particles while the experiment is taking place.

The skimmer is simply a reservoir (bottle) placed slightly below the water's surface. Water is removed from the bottle via a tube connected to an intake to the pump. The rate of water entering the bottle is determined by the angle of the bottle. The apparatus is self adjusting (through a competition of buoyancy forces and counter weights) to the pump speed. The main function of the bottle is to produce a water level lower than that of the surface. The fluid from the surface is then drawn in trapping any surface contaminants.

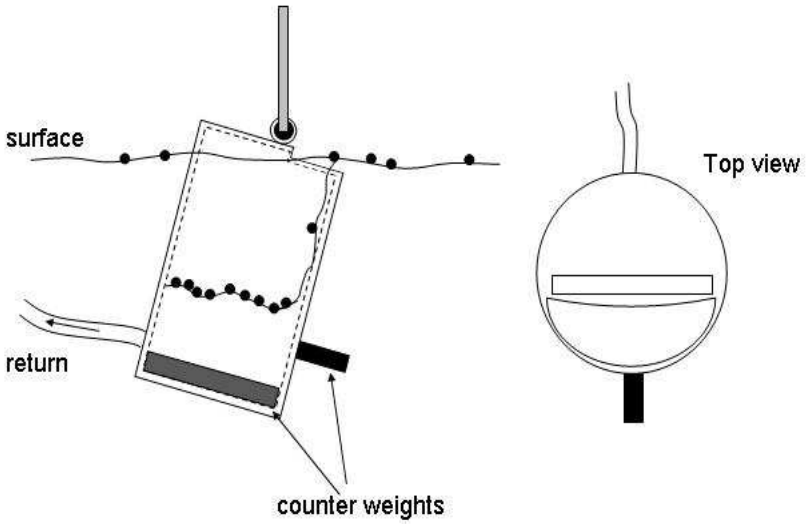

Figure 27: Schematic of the skimming device used to clean the surface. The device is a cylindrical plastic jar, with a section of the top removed to allow the flow of water into the reservoir. A large weight is placed in the bottom of the jar to counteract buoyancy forces, while a second smaller weight is attached to the outside to give the jar a preferred tilt. Water is removed from the skimmer through a latex tube, which is inserted into one of four pipes recirculating water back to the pump.

APPENDIX D

COMPUTER EXPERIMENTS

The computer simulation performed by Joerg Schumacher and Bruno Eckhardt model a turbulent shear flow bounded by two stress-free surfaces taken to be planes perpendicular to the z direction. A pseudospectral method is used to integrate the Navier-Stokes equation[73] and the velocity field is decomposed in a Fourier expansion[22]. The boundary conditions for the free-surface, at $z = 0$ and $z = 1$ are give as

$$\partial_z u = \partial_z v = w = 0 \tag{D.1}$$

These boundary conditions can be taken into account by using the following Fourier decomposition.

$$u(x, y, z, t) = \sum_{\tilde{\mathbf{K}},n} u_{\tilde{\mathbf{K}},n}(t) exp(i\tilde{\mathbf{K}} \cdot \tilde{\mathbf{x}}) cos(n\pi z), \tag{D.2}$$

$$v(x, y, z, t) = \sum_{\tilde{\mathbf{K}},n} v_{\tilde{\mathbf{K}},n}(t) exp(i\tilde{\mathbf{K}} \cdot \tilde{\mathbf{x}}) cos(n\pi z), \tag{D.3}$$

$$w(x, y, z, t) = \sum_{\tilde{\mathbf{K}},n} w_{\tilde{\mathbf{K}},n}(t) exp(i\tilde{\mathbf{K}} \cdot \tilde{\mathbf{x}}) sin(n\pi z), \tag{D.4}$$

The variables with tildes are restricted to plane of surface taken to be $z = 1$. Here $\tilde{\mathbf{K}}$ are all of the two-dimensional wave vectors in the surface. The velocity determined in this manner

allows for the direct study of the motion of tracer particles in the surface. The boundary conditions at the surface ensure that particles can neither enter nor leave the surface.
Periodic boundaries apply in the two directions parallel to the surface. The aspect ratio of the system is $L_x : L_y : L_z = 2\pi : 2\pi : 1$ with a resolution of 256 by 256 by 65. All measurements are made dimensionless by dividing by the appropriate Kolmolgorov length or time scale, $\eta = (\nu^3/\epsilon)^{1/4}$ or $\tau_\eta = (\nu/\epsilon)^{1/2}$. The dissipation rate, ϵ is determined from the simulated velocity gradient on the surface.

APPENDIX E

THE FLUCTUATION THEOREM

This section is devoted to outlining the basic assumptions and results of the Gallavotti and Cohen fluctuation theorem (FT). As stated above, this theory attempts to construct an ensemble measure that may be used to obtain time-averaged global quantities. The proposed measure is the "Sinai-Ruelle-Bowen" (SRB) distribution, now to be defined.

Any driven system held in a steady state must have a dissipative element, which is reflected in phase space by a positive contraction rate. Therefore any initial distribution in phase space will, under the action of the system's dynamics, ultimately collapse to a zero volume distribution. This zero volume distribution, or attractor, is the analog to the discrete equal probability distribution in equilibrium mechanics. It is important to note that although the system is dissipative the equations of motion are time reversible. This property implies that for every state x on the attractor there exist a second state x', also on the attractor whose dynamics are simply the time reversal of x.

The GC theory is predicated on the chaotic hypothesis which states that a many body system in a stationary state can be modelled as a transitive Anosov system in order to measure macroscopic quantities[74, 75]. A transitive Anosov system is a smooth system where one can define a local coordinate system about any point, x, in phase space. This local coordinate system must follow x as it travels through phase space. In addition, every point in phase space must be hyperbolic. The plane in phase space perpendicular to the motion of x is filled with points moving towards, and points moving away from x, composing the stable and unstable coordinate surfaces(manifolds). One can think of the density of points on these

surfaces as an inverse of the volume along the respective manifolds. Therefore as the system evolves one can define a rate of change of volume, which will be denoted as σ.

Steady state phase space will then look like infinitely thin multidimensional sheets which are smooth along the unstable manifold. The SRB measure is then a distribution which is necessarily continuous along the unstable directions, and discrete along the stable ones.

Without loss of generality, continuous temporal evolution can be replaced with a time map S^t. Phase space is also sectioned into discrete cells, E_i, whose size can be made as small as one wishes by taking the intersection of cells formed by applications of the time map and its inverse[57]. Typically the size should be made small enough to have little variation in the physical quantity of interest over the points in the cell. Using this recipe one can define the SRB measure for any physical observable:

$$\langle F \rangle = \int_\omega F(y)\mu dy = \frac{\sum_{E_i} \Lambda_{u,T}^{-1}(x_i)F(x_i)}{\sum_{E_i} \Lambda_{u,T}^{-1}(x_i)} \tag{E.1}$$

Here Λ is the phase space contraction rate, and the subscript u stands for the the unstable manifold. Therefore the probability of an individual state is proportional to the inverse of the volume increase on the unstable manifold over the time T. In other words, the more unstable a state is the less likely it will be occupied. Strictly speaking, the above relation becomes exact when T goes to infinity.

The total phase space contraction rate, σ, is of particular interest($\sigma(x) = -log(\Lambda(x))$). Here λ is the Jacobian of the time map, which is a measure of the the volume change of the space about x under the action of S. The ensemble, or infinite time average of the phase space contraction rate is given by $\sigma_+ = \int_\Gamma \sigma(y)\mu dy$, which is necessarily positive for dissipative systems. The time average of σ is given by, $s_\tau = (1/\tau)\sum_{k=-\tau/2}^{\tau/2} \sigma(S^k x)$. Here T is much longer then the averaging time τ, which can be interpreted experimentally as the measurement time.

In order to establish the relative probabilities of positive to negative entropy production rates we take the ratio of their SRB measures.

$$\frac{\pi(s_\tau)}{\pi(-s_\tau)} = \frac{\sum_{E_i;s_\tau} \Lambda_{u,T}^{-1}(x_i)}{\sum_{E_i;-s_\tau} \Lambda_{u,T}^{-1}(x_i)} \tag{E.2}$$

By making the approximation that the time T is taken to be equal to τ, the weights are measured over the same time as s_τ. By making this change of limits we are no longer using the true SRB measure which, as stated above, is only precise when T goes to infinity[74]. However by performing this approximation and making use of the systems Time reversal invariance one can replace the contraction along the unstable manifold over cells with entropy production rate $-s_\tau$ in the denominator with the expansion rate over the stable manifold for the same cells in the numerator.

Therefore for each cell we are left with $\Lambda_{u,T}^{-1}(x_i)\Lambda_{s,T}^{-1}(x_i)$. The *log* of this quantity with $T = \tau$ is taken to be equivalent to $\sum_{k=-\tau/2}^{\tau/2}\sigma(S^k x) = s_\tau\tau$ the total phase space contraction rate times τ and therefore the same for all points in the sum[74]. Equating this product to the total contraction rate is permitted by the construction of an Anosov system. By making the substitutions $\Lambda_{u,T}^{-1}(x_i) = ab(x_i)$, $\Lambda_{s,T}(x_i) = b(x_i)/c$, and $ac = e^{s_\tau\tau}$ the ratio of sums simplifies to the following relation.

$$\frac{\sum_{E_i;s_\tau}\Lambda_{u,\tau}^{-1}(x_i)}{\sum_{E_i;s_\tau}\Lambda_{u,\tau}(x_i)} = \frac{\sum_{E_i;s_\tau}ab(x_i)}{\sum_{E_i;s_\tau}b(x_i)/c} = ac\frac{\sum_{E_i;s_\tau}b(x_i)}{\sum_{E_i;s_\tau}b(x_i)} = e^{s_\tau\tau} \tag{E.3}$$

Which leaves us with the main prediction of the GC theory, the Fluctuation Theorem:

$$\pi(s_\tau)/\pi(-s_\tau) = e^{\tau s_\tau} \tag{E.4}$$

There are some difficulties in the change of limits, and this is discussed in detail in reference [74].

This result predicts a finite probability for the existence of negative contraction rates, and more importantly negative entropy production. As would be expected the the relative probability for such events decreases for longer measurement times τ.

Bibliography

BIBLIOGRAPHY

[1] M. C. Facchini, M. Mircea, S. Fuzzi, and R. J. Charlson. *Nature*, 401:257, 1999.

[2] R. A. Shaw. *Annu. Rev. Fluid Mech*, 35:183, 2003.

[3] H.Stommel. *J. Marine Research*, 8:199, 1949.

[4] R. E. Davis. *Annu. Rev. Fluid Mech.*, 23:43, 1991.

[5] J. Schumacher and B. Eckhardt. *Phys. Rev. E*, 66:017303, 2002.

[6] U. Frisch. *Turbulence*. Cambridge UniversityPress, Cambridge,Ma, 1995.

[7] A. Kolmogorov. Dissipation of energy in a locally isotropic turbulence. *Doklady Akad. Nauk SSSR*, 32:141, 1941.

[8] S. Grossman and I. Procaccia. *J. Marine Research*, 29:1358, 1984.

[9] N. Matsunaga *et al. Fluid Dyn. Res.*, 25:147, 1999. his reference contains a complete-bibliography of prior experiments on oscillating grid turbulence.For related studies of particle motion near the surface in channelflow, see Y. Pan and S. Banerjee Phys. Fluids **7**, 1649(1995) and S. Kumar, R. Gupta, and S. Banerjee, Phys. Fluids **10**, 437 (1991).

[10] B. W. Zeff, R. McAllister D. D. Lanterman, R. Roy, E. J. Kostelich, and D. P. Lathrop. *Nature*, 421:146, 2003.

[11] Private communication with g. boffetta.

[12] W.I. Goldburg, J.R. Cressman, Z. Voros, B. Eckhardt, and J. Schumacher. *Phys. Rev. E*, 63:065303, 2001.

[13] G. Falkovich, K. Gawedzki, and M. Vergassola. *Rev. Mod. Phys.*, 73:913, October 2001.

[14] A. Pumir, B. I. Shraiman, and M. Chertkov. *Phys. Rev Lett*, 85:5324, 2000.

[15] P. Castglione and A. Pumir. *Phys. Rev. E*, 64:056303, 2001.

[16] M.-C. Jullien, J. Paret, and P. Tabeling. *Phys. Rev. Lett.*, 82:2872, 1999.

[17] G. Boffetta and A. Celani. *Physica A*, 280:1, 2000.

[18] G. Boffetta, A. Celani, A. Crisanti, and A. Vulpiani. *Phys. Rev. E*, 60:6734, 1999.

[19] E. Schroder. *Phys. Rev. Lett.*, 76:4717, 1996.

[20] E. Schroder and P. Alstrom. *Phys. Rev. E*, 57:7329, January 1998.

[21] K. Gawędzki and M. Vergassola. *Physica D*, 183:63, 2000.

[22] B. Eckhardt and J. Schumacher. *Phys. Rev. E*, 64:016314, 2001.

[23] J.R. Cressman, W.I. Goldburg, and J. Schumacher. *submitted to Europhys. Lett*, 2003.

[24] A. Celani, A. Lanotte, A. Mazzino, and M. Vergassola. *Phys. Rev. Lett*, 84:2385, 2002.

[25] H. Schlichting. *Boundary-Layer Theory*. McGraw-Hill, NewYork, 6th ed. edition, 1968.

[26] A. Gyr and H.-W Bewersdorff. Kluwer Academic, Boston, 1995.

[27] J.R. Cressman, Q. Bailey, and W.I. Goldburg. Modification of a vortex street by a polymer additive. *Phys. Fluids*, 13:867, 2001.

[28] M. Provansal, C. Mathis, and L. Boyer. *J. Fluid Mech.*, 182:1, 1987.

[29] K. R. Sreenivasan, P. J. Strykowski, and D. J. Olinger. *Proc.on Unsteady Flow Separation*, page 1, 1986. edited by K. N. Ghia,ASME.

[30] F. James and A. J. Acosta. *J. Fluid Mech.*, 42:269, 1970.

[31] N. Kalashnikov and A. M. Kudin. *Nature*, 225:445, 1970.

[32] Delvaux and M. J. Crochet. *J. Non-Newtonian Fluid Mech.*, 37:297, 1990.

[33] O. Cadot, D. Bonn, and S. Douady. *Phys. Fluids*, 47:10, 1998.

[34] W. I. Goldburg P. Tong and J. S. Huang. *Phys. Rev. A*, 45:7231, 1992.

[35] H. K. Williamson. *Annu.Rev. Fluid Mech.*, 28:477, 1996.

[36] J. Olinger and K. R. Sreenivasan. *Phys. Rev. Lett.*, 60:797, 1988.

[37] O. Cadot and M. Lebey. *Phys. Fluids A*, 28:477, 1996.

[38] M. A. Rutgers, X. L. Wu, R. Bagavatula, A. A. Peterson, and W. I.Goldburg. *Phys. Fluids*, 8:2847, 1997.

[39] M. Beizaie and M. Gharib. *Exp. Fluids*, 23:130, 1997.

[40] Gharib and P. Derango. *Physica D*, 37:406, 1989.

[41] M. Rivera, P. Vorobieff, and R. Ecke. *Phys. Rev. Lett.*, 81:1417, 1998.

[42] P. Vorobieff, M. Rivera, and R. E. Ecke. *Phys. Fluids*, 11:2167, 1999.

[43] Y. Couder, J.-M. Chomaz, and M. Rabaud. *Physica D*, 37:384, 1999.

[44] In a soap film, the transition to vortex shedding is hysteretic. See V. K.Horvath, J. R. Cressman, W. I. Goldburg, and X. L. Wu, Phys. Rev. E61, R4702 2000.

[45] Dawn is a Proctor and Gamble product.

[46] Model DV-111, Brookfield Eng. Labs., Stoughton, MA.

[47] G.K. Batchelor. *An Introduction to Fluid Dynamics*. Cambridge University Press, Cambridge, 1969.

[48] P. W. Bearman. *J. FluidMech.*, 21:241, 1965.

[49] H. Usui, T. Shibata, and Y. Sano. *Chem. Eng. J. Japan*, 13:77, 1980.

[50] Horace Lamb. *Hydronamics*. Dover, NewYork, 6th ed. edition, 1945.

[51] S.T. Bramwell et al. *Nature*, 396:552, 1998.

[52] S.T. Bramwell et al. *Phys. Rev. Lett.*, 84:3744, 2000.

[53] S.T. Bramwell et al. *Europhys. Lett.*, 57:310, 2002.

[54] D.J. Evans et al. *Phys. Rev. Lett.*, 71:2401, 1993.

[55] G.M. Wang et al. *Phys. Rev. Lett.*, 89:050601, 2002.

[56] S. Aumaitre et al. *Eur. Phys. J.*, B19:449, 2001.

[57] G. Gallavotti and E.G.D. Cohen. *Phys. Rev. Lett.*, 74:2694, 1995.

[58] K. Huang. *Statistical Mechanics*. Wiley, New York, 2nd ed. edition, 1987.

[59] G. E. Crooks. *Rev. E*, 60:2721, 1999.

[60] P.G De Gennes and J. Prost. *The Physics of Liquid Crystals*. Clarendon Press, Oxford, 2nd ed. edition, 1993.

[61] T. Toth-Katona, J.R. Cressman, W.I. Goldburg, and J.T. Gleeson. *Phys. Rev. E*, 68:030101, 2003.

[62] P. Coullet, L. Gil, and J. Lega. *Phys. Rev. Lett.*, 62:1619, 1989.

[63] S. Kai and W. Zimmerman. *Prog. Theor. Phys. Suppl*, 99:458, 1989.

[64] Product of Merck Co.

[65] J.Shi, C. Wang, V. Surendranath, K. Kang, and J.T. Gleeson. *Liq. Cryst.*, 29:877, 2002.

[66] S. Kai and K. Hirakawa. *Prog. Theor. Phys. Suppl*, 64:212, 1978.

[67] S. Nasuno, O. Sasaki, S. Kai, and W. Zimmerman. *Phys. Rev. A.*, A46:4954, 1992.

[68] S. Kai, M. Araoka, H. Yamazaki, and K. Hirakawa. *J. Phys. Soc. Jpn.*, 46:393, 1979.

[69] G. Goren, I. Procaccia, S. Rasenat, and V. Steinberg. *Phys. Rev. Lett.*, 63:1237, 1989.

[70] W.I. Goldburg, Y.Y. Goldschmidt, and H. Kellay. *PRL*, 87:245502, 2001.

[71] E. Villermaux. *Phys. Rev. Lett*, 75:4618, 1995.

[72] Private communication from Charles Knobler.

[73] J. Schumacher and B. Eckhardt. *Europhys. Lett.*, 52:627, 2000.

[74] G. Gallavotti. *Chaos*, 8:384, 1995.

[75] E. Cohen. *Physica A*, 240:43, 1997.